
# Materials and Device Engineering for Efficient and Stable Polymer Solar Cells

Rickard Hansson

Faculty of Health, Science and Technology

Physics

DOCTORAL THESIS | Karlstad University Studies | 2017:2

# Materials and Device Engineering for Efficient and Stable Polymer Solar Cells

Rickard Hansson

DOCTORAL THESIS | Karlstad University Studies | 2017:2

Materials and Device Engineering for Efficient and Stable Polymer Solar Cells

Rickard Hansson

DOCTORAL THESIS

Karlstad University Studies | 2017:2

urn:nbn:se:kau:diva-47257

ISSN 1403-8099

ISBN 978-91-7063-736-0 (print)

ISBN 978-91-7063-739-1 (pdf)



Distribution:
Karlstad University
Faculty of Health, Science and Technology
Department of Engineering and Physics
SE-651 88 Karlstad, Sweden
+46 54 700 10 00

Print: Universitetstryckeriet, Karlstad 2017

WWW.KAU.SE

*Utan tvivel är man inte klok*

Tage Danielsson

## Abstract

Polymer solar cells form a promising technology for converting sunlight into electricity, and have reached record efficiencies over 10% and lifetimes of several years. The performance of polymer solar cells depends strongly on the distribution of electron donor and acceptor materials in the active layer. To achieve longer lifetimes, degradation processes in the materials have to be understood. In this thesis, a set of complementary spectroscopy and microscopy techniques, among which soft X-ray techniques have been used to determine the morphology of polymer:fullerene based active layers. We have found that the morphology of TQ1:$PC_{70}BM$ films is strongly influenced by the processing solvent and the use of solvent additives. We have also found, by using soft X-ray techniques, that not only the light-absorbing polymer TQ1, but also the fullerene is susceptible to photo-degradation in air. Moreover, the fullerene degradation is accelerated in the presence of the polymer. Additionally, this thesis addresses the role of the interfacial layers for device performance and stability. The commonly used hole transport material PEDOT:PSS has the advantage of being solution processable at room temperature, but this layer is also known to contribute to the device degradation. We have found that low-temperature processed $NiO_x$ is a promising alternative to PEDOT:PSS, leading to improved device performance. Even for encapsulated polymer solar cells, some photo-induced degradation of the electrical performance is observed and is found to depend on the nature of the hole transport material. We found a better initial stability for solar cells with $MoO_3$ hole transport layers than with PEDOT:PSS. In the pursuit of understanding the initial decrease in electrical performance of PEDOT:PSS-based devices, simulations were performed, from which a number of degradation sources could be excluded.

## List of publications

The thesis is based on the following papers:

I. *Vertical and lateral morphology effects on solar cell performance for a thiophene-quinoxaline copolymer:$PC_{70}BM$ blend,*
R. Hansson, L. K. E. Ericsson, N. P. Holmes, J. Rysz, A. Opitz, M. Campoy-Quiles, E. Wang, M. G. Barr A. L. D. Kilcoyne, X. Zhou, P. Dastoor, E. Moons
*Journal of Materials Chemistry A*, **2015**, 3, 6970-6979.

II. *Photo-degradation in air of the active layer components in a thiophene-quinoxaline copolymer:fullerene solar cell,*
R. Hansson, C. Lindqvist, L. K. E. Ericsson, A. Opitz, E. Wang, E. Moons
*Physical Chemistry Chemical Physics,* **2016**, 18, 11132.

III. *Low temperature processed $NiO_x$ hole transport layers for efficient polymer solar cells,*
S. D. Chavhan, R. Hansson, L. K. E. Ericsson, P. Beyer, A. Hofmann, W. Brütting, A. Opitz, E. Moons
*Submitted manuscript*

IV. *Opportunities and challenges in probing local composition of organic material blends for photovoltaics,*
R. Hansson, L. K. E. Ericsson, N. P. Holmes, V. Blazinic, P. Dastoor, E. Moons
*Submitted manuscript*

V. *The role of the hole transport layer in the initial photo-degradation of PCDTBT:$PC_{70}BM$ solar cells*,
S. Züfle, R. Hansson, E. A. Katz, E. Moons, B. Ruhstaller
*Manuscript*

## Contribution report

I. Prepared all samples except for ellipsometry. Carried out all measurements and analysis except for ellipsometry and SIMS. Wrote the paper.

II. Prepared all samples and carried out all measurements except for UV-Vis spectroscopy. Analysed all the data. Wrote the paper.

III. Prepared samples together with S. D. Chavhan. Carried out all measurements and analysis except for EQE and Kelvin probe. Wrote the majority of the manuscript.

IV. Prepared all samples. Carried out all measurements and analysis except for electron microscopy. Wrote the first draft of the manuscript and prepared the final version in collaboration with the coauthors.

V. Prepared all samples. Carried out measurements and analysis of the results at 1 sun. The numerical simulations and the experiments under concentrated sunlight were performed by S. Züfle. Wrote the manuscript together with S. Züfle.

## Related publications not included in this thesis

VI. *$V_{OC}$ from a Morphology Point of View: the Influence of Molecular Orientation on the Open Circuit Voltage of Organic Planar Heterojunction Solar Cells,*
U. Hörmann, C. Lorch, A. Hinderhofer, A. Gerlach, M. Gruber, J. Kraus, B. Sykora, S. Grob, T. Linderl, A. Wilke, A. Opitz, R. Hansson, A. Anselmo, Y. Ozawa, Y. Nakayama, H. Ishii, N. Koch, E. Moons, F. Schreiber, W. Brütting
*Journal of Physical Chemistry C*, **2014**, 118, 26462-26470.

VII. *The influence of oxygen adsorption on the NEXAFS and core-level XPS spectra of the $C_{60}$ derivative PCBM*,
I. E. Brumboiu, L. K. Ericsson, R. Hansson, E. Moons, O. Eriksson, B. Brena
*Journal of Chemical Physics*, **2014**, 142, 054306.

VIII. *Fluorescence Spectroscopy Studies on Polymer Blend Solutions and Films for Photovoltaics*,
J. van Stam, R. Hansson, C. Lindqvist, L. K. Ericsson, E. Moons
*Colloids and Surfaces A: Physicochem. Eng. Aspects*, **2015**, 483, 292-296.

IX. *Fluorescence and UV/Vis absorption spectroscopy studies on polymer blend films for photovoltaics,*
J. van Stam, C. Lindqvist, R. Hansson, L. K. Ericsson, E. Moons.
*Proceedings of SPIE*, **2015**, 9549, 95490L.

X. *Organic heterojunctions: Contact-induced molecular reorientation, interface states, and charge re-distribution,*
A. Opitz, A. Wilke, P. Amsalem, M. Oehzelt, R.- P. Blum, J. P. Rabe, T. Mizokuro, U. Hörmann, R. Hansson, E. Moons, N. Koch.
*Scientific Reports*, **2016**, 6, 21291.

XI. *Efficient ternary organic solar cells based on immiscible blends*,
J. Farinhas, R. Oliveira, R. Hansson, L. K. Ericsson, E. Moons, J. Morgado, A. Charas.
*Organic Electronics*, **2017**, 41, 130-136.

XII. *C1s NEXAFS Investigations of $PC_{60}BM$ Exposed to Oxygen: a Novel Approach for the Comparison of Computed and Experimental Spectra*,
I. E. Brumboiu, L. K. E. Ericsson, V. Blazinic, R. Hansson, E. Moons, B. Brena.
*Manuscript*

XIII. *Spectroscopy of Photo-Oxidized $PC_{60}BM$*,
L. K. E. Ericsson, I. E. Brumboiu, V. Blazinic, R. Hansson, C. Lindqvist, B. Brena, E. Moons.
*Manuscript*

## Acknowledgements

First of all, I would like to thank my supervisor Ellen Moons and co-supervisor Andreas Opitz for all the guidance, support and encouragement. I would also like to thank Jan van Stam, Leif Ericsson, Vanja Blazinic, Camilla Lindqvist, Sudam Chavhan, and Ana Sofia Anselmo. You have all provided an excellent atmosphere to perform research in and I have thoroughly enjoyed my time working together with you.

I would like to thank my colleagues at the Department of Engineering and Physics for making my time here pleasant.

I wish to thank Paul Dastoor, Natalie Holmes, and Xiaojing Zhou, for introducing me to the STXM technique and also for the nice time spent together in Berkeley.

I would like to thank Ulrich Hörmann, Ergang Wang, Christian Müller, Jakub Rysz, Monika Biernat, Jasper Michels, Barbara Brena, Iulia Brumboiu, Mariano Campoy-Quiles, Simon Züfle, Paul Beyer and Alexander Hofmann. This work would not have been what it is without your help.

Many thanks to Alexei Preobrajenski, Alexander Generalov, Ben Watts, and David Kilcoyne for all the help during synchrotron beamtimes.

Last, but certainly not least, I would like to thank my family and friends for making sure that my time spent outside the confines of the laboratory also has been pleasant.

## List of acronyms

| | |
|---|---|
| AEY | Auger electron yield |
| AFM | Atomic force microscopy |
| AM1.5 | Air mass 1.5 |
| EELS | Electron energy loss spectroscopy |
| EQE | External quantum efficiency |
| FF | Fill factor |
| HOMO | Highest occupied molecular orbital |
| HTL | Hole transport layer |
| IQE | Internal quantum efficiency |
| ITO | Indium doped tin oxide |
| $J_{SC}$ | Short circuit current |
| LUMO | Lowest unoccupied molecular orbital |
| MDMO-PPV | Poly[2-methoxy-5-(3',7'-dimethyloctyloxy)-1,4-phenylenevinylene] |
| MPP | Maximum power point |
| NEXAFS | Near-edge X-ray absorption fine structure |
| P3HT | Poly(3-hexylthiophene) |
| PCBM, $PC_{60}BM$ | [6,6]-phenyl-$C_{61}$-butyric acid methyl ester |
| $PC_{70}BM$ | [6,6]-phenyl-$C_{71}$-butyric acid methyl ester |
| PCDTBT | Poly[N-(1-octylnonyl)-2,7-carbazole]-alt-5,5-[4',7'-di(thien-2-yl)-2',1',3'-benzothiadiazole] |
| PCE | Power conversion efficiency |
| PEDOT:PSS | Poly(3,4-ethylenedioxythiophene) polystyrene sulfonate |
| PET | Polyethylene terephthalate |
| PEY | Partial electron yield |
| SEM | Scanning electron microscopy/microscope |
| SIMS | Secondary ion mass spectrometry |
| STM | Scanning tunneling microscopy |
| STXM | Scanning transmission X-ray microscopy |
| TQ1 | Poly[2,3-bis-(3-octyloxyphenyl)quinoxaline-5,8-diyl-alt-thiophene-2,5-diyl] |
| TEM | Transmission electron microscopy/microscope |
| TEY | Total electron yield |
| UPS | Ultraviolet photoelectron spectroscopy |
| $V_{OC}$ | Open circuit voltage |
| XPS | X-ray photoelectron spectroscopy |

## Contents

# Chapter 1
# Introduction

Since the industrial revolution two centuries ago, the world has seen a tremendous increase in energy consumption. In 2010 the total global energy need was 17.5 TW and has been predicted to grow to 27.4 TW by 2040.[1] A significant part of that energy has so far come from burning fossil fuels. Environmental issues associated with fossil fuels aside, at the current consumption rate it is only a matter of time before easily attainable fossil fuel sources are depleted. In order to meet the demands for energy in the future, alternative sources of energy must be utilized more.

By far the largest source of energy currently available on Earth is sunlight. The sun transfers 1.36 kW/m$^2$ to the outer atmosphere[2] which leaves, after accounting for energy losses due to sunlight being reflected and absorbed by the atmosphere, enough power that the sunlight hitting the surface of the Earth in one and a half hour exceeds the world's annual energy consumption.[3] It is of course unfeasible to capture all of that energy, but the sheer amount of available energy alone shows that merely a small fraction would be enough for conversion to desired energy forms.

There exists a multitude of ways in which the power from sunlight can be harnessed. Green plants and cyanobacteria convert solar energy into chemical energy through photosynthesis. Sunlight unevenly heating the surface of the Earth creates pressure differences that set air in motion, creating wind, a form of kinetic energy. Sunlight also heats the oceans causing water to evaporate, allowing it to later fall out of the atmosphere as precipitation and accumulate in e.g. dams, a form of potential energy. To produce electricity, these aforementioned forms of energy would need to be converted further, and involves additional energy losses of varying degree which not seldom require rather bulky equipment. Solar cells, on the other hand, provide means to convert the energy of light into electrical energy in a one-step process.

The first observation of an electrical current being generated in a material by light exposure was made in 1839 by Becquerel working on silver coated platinum electrodes in electrolytes.[4] In 1873 photoconductivity was discovered by Smith in selenium[5] and in 1883 a solar cell made from gold coated selenium was built by Fritts that had a power conversion efficiency (PCE) of 1%.[6] Due

to the high material cost and the low PCE, this kind of solar cell never found use in any large scale power generation. The next big step in the development of solar cell technology was taken in 1954 at Bell Labs when the first silicon solar cell displaying a PCE of 6% was developed.[7] As of today, silicon solar cells are by far the most prevalent type of solar cell with the record efficiency just above 25% for monocrystalline silicon.[8]

For the last two decades there has been an exponential increase in electrical power produced by solar cells, increasing from 0.1 GW in 1992 to at least 134 GW in 2013.[9] Arguably one of the most important reasons for this increased solar cell usage is the reduction in production costs and various national measures of economic support for the end users. Despite that, power from solar cells still accounts for less than 1% of the total global power production.

For any type of solar cell to become more commercially viable, efficiencies need to increase or fabrication costs need to decrease. Today the best performing silicon solar cells have a PCE that is not very far from the theoretical limit for single junction devices, known as the Shockley-Quessier limit, which is 30% for silicon.[10] This means that the potential benefits that could be had by reducing the fabrication costs are greater than those from improving the efficiency.

In order to reduce the production costs, several alternative solar cell technologies have been developed over the years. Particularly promising are organic solar cells, mainly because of the compatibility with inexpensive printing techniques, similar to those used to print newspapers.[11] The mechanical flexibility and low weight together with the chemically tunable properties of organic materials allow for novel applications such as integration with textiles[12] and transparent solar cells.[13]

Currently the record PCE for organic solar cells has reached 11.1%.[8] This progress is the result of great effort, largely owing to the development of new photoactive materials,[14] but also to the increasing understanding of and control over the morphology of the solar cell's active layer.[15-18]

No matter how efficient a solar cell is or how inexpensive it is to produce, it will never see any widespread use unless the lifetime also is reasonably long. As it stands today, device stability is one of the greater challenges that organic solar cells face. For printed organic solar cells to be able to compete with silicon, it is

estimated that a module PCE of 7% and 5 years lifetime would be sufficient.[19] With the record PCE for mini modules currently at 9.5%[8] and record outdoor lifetimes of modules surpassing two years,[20] we are now at a point where it has become at least as important to improve the lifetime as it is to improve the PCE. Further improvement requires an increased understanding of the fundamental processes behind efficiency and stability.

This thesis presents the use of complementary spectroscopy and microscopy methods to probe the local composition in the active layer of polymer solar cells. The stability of the active layer is studied and the interplay between the photo-degradation of donor and acceptor molecules is investigated. Additionally, this thesis addresses how the interfacial layers between the active layer and the electrodes can influence device performance and stability.

# Chapter 2
# Polymer solar cells

## 2.1 Organic semiconductors

Although organic electronics is a relatively new technology, semiconducting properties of organic materials were discovered already in 1906 when Pochettino observed photoconductivity in anthracene.[21] Anthracene was also the first organic material in which the photovoltaic effect was observed,[22] although with a PCE on the order of $10^{-6}$. The first polymer to display photoconductivity, polyvinyl-carbazole, was described in 1957 by Hoegl et al.[23, 24] A breakthrough was made in 1977 when Heeger, MacDiarmid and Shirakawa discovered and developed conducting, conjugated polymers,[25, 26] which they were awarded the Nobel Prize in Chemistry for in 2000. Ever since, there has been a growing interest in optoelectronic technology based on organic semiconductors.

The difference between a semiconducting and a non-conducting polymer lies in the nature of the chemical bonds along the molecule backbone. Single bonds normally consist of σ-bonds formed by head-on overlap of atomic or hybrid orbitals. Electrons that take part in σ-bonds are localized and unable to move along the molecular backbone; hence a polymer with only single bonds along the backbone will be an electrical insulator. If instead, there are alternating single and double bonds (*i.e.* a conjugated system), each carbon atom along the backbone will form three $sp^2$ hybridized orbitals and one unhybridized p-orbital. The overlapping $sp^2$ orbitals form σ-bonds and the overlapping p-orbitals form π-bonds (see Figure 2.1.1). In contrast to σ-bonds, electrons partaking in π-bonds are delocalized and overlap of the π-orbitals allows them to be delocalized along the conjugated backbone. When the two p-orbitals combine, a lower energy, bonding π-molecular orbital as well as a higher energy, antibonding π*-molecular orbital can be formed.[27, 28] The energy difference between the highest occupied molecular orbital (HOMO) and the lowest unoccupied molecular orbital (LUMO) determines the HOMO-LUMO gap and is for conjugated polymers usually in the range of 1-4 eV,[29] in other words, in the same range as the bandgap of inorganic semiconductors.

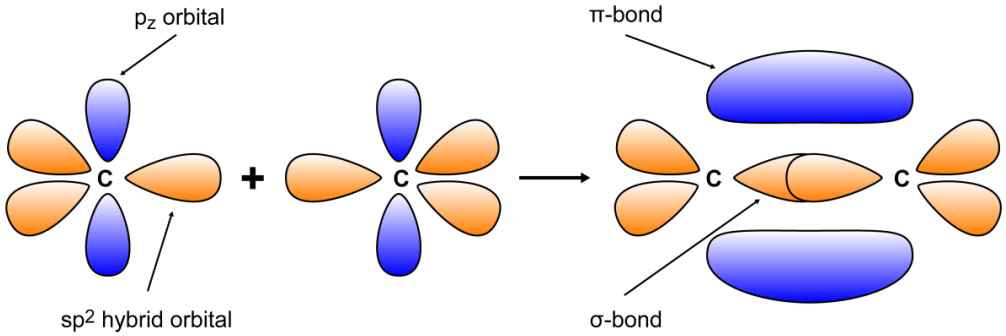


**Figure 2.1.1.** Formation of σ- and π-bonds in a carbon-carbon double bond.

There are several fundamental differences between organic and inorganic semiconductors. In contrast to inorganic semiconductors, every molecule in an organic semiconductor is an individual semiconductor. Unless the material is ordered and ultrapure, electrical transport requires the charge carriers to be thermally activated in order to move from molecule to molecule by hopping.[30] Consequently, the charge carrier mobility in organic semiconductors is much lower than in most inorganic semiconductors. On the other hand, the absorption coefficients of organic semiconductors are relatively large. For solar cell applications, low charge carrier mobilities can therefore, at least partly, be compensated for by using thin films (~100 nm) that still give high light absorption.[31]

Another important difference between organic and inorganic semiconductors is related to excitons. An exciton is a quasiparticle created upon light absorption and consists of an excited electron and hole held together by Coulomb forces. Since organic materials generally have a low dielectric permittivity, the screening of charges is weaker and the exciton binding energy higher than for inorganic materials. Inorganic materials have exciton binding energies low enough that the thermal energy available at room temperature of about 25 meV is sufficient to dissociate the exciton into free charges, whereas organic materials typically have exciton binding energies in the range of 0.5-1 eV,[32] and hence cannot be dissociated by thermal excitation alone.[33]

## 2.2 Device operation

A polymer solar cell is a layered structure (see Figure 2.2.1), where the organic photoactive layer, often along with interlayers, is sandwiched between two electrodes. At least one of the electrodes needs to be transparent for obvious reasons. Commonly used transparent electrodes include indium doped tin oxide (ITO) or metal grids.

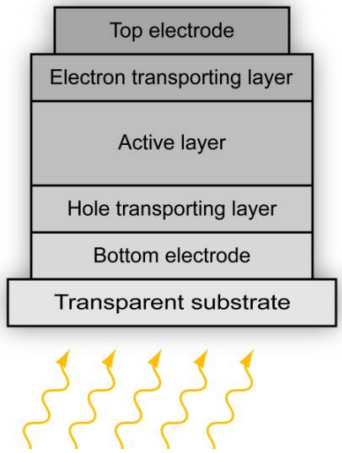


**Figure 2.2.1.** Typical organic solar cell device structure.

As mentioned previously, the exciton binding energy in organic materials is high compared to the thermal energy at room temperature. A common approach to dissociate the excitons is through the use of two different materials that form a heterojunction. For this to be effective there should be a LUMO-LUMO and a HOMO-HOMO energy level offset between the two materials that provide enough driving force for the exciton dissociation, and additionally the energy levels should be such that a staggered (type II) heterojunction is formed (see Figure 2.2.2). The material with the higher LUMO energy level will act as an electron donor and the other material as an electron acceptor. That way, if light is absorbed in the donor, the exciton can be dissociated by the transfer of an electron from the donor to the acceptor, and if light is absorbed in the acceptor, the exciton can be dissociated by the transfer of a hole from the acceptor to the donor. This, however, requires that the exciton is able to reach the donor/acceptor interface before it recombines and the absorbed energy is lost as heat. The exciton diffusion length in organic materials is about 5-20 nm,[34-37] so efficient exciton dissociation also relies on the distribution of donor and acceptor materials (*i.e.* the morphology) being such that ideally everywhere

in the photoactive layer there is a donor/acceptor interface within the exciton diffusion length.

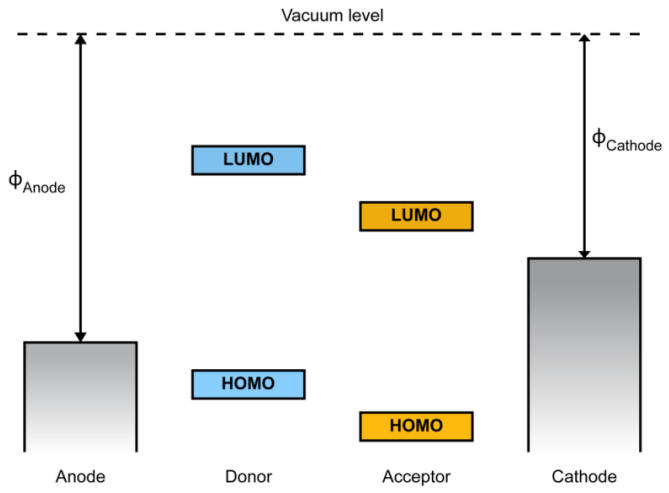


**Figure 2.2.2.** Energy levels of the donor, acceptor and electrodes of an organic solar cell, before electrical contact has been made.

Upon reaching the donor/acceptor interface, the exciton is however not immediately separated into free charges, but forms an interfacial state known as a charge transfer (CT) state.[38, 39] In the CT state, the electron in the acceptor and the hole in the donor are still loosely bound at the donor/acceptor interface, but the binding energy is low enough for the charges to separate at room temperature.[40]

After having been successfully dissociated into free charges, the next step is for the charges to reach the electrodes. The driving force for the charge transport is provided by the internal electric field produced by the use of electrodes with different work functions. Also in this step, the morphology is of great importance. Since the electrons mainly move through the acceptor material and the holes through the donor material, continuous pathways of either material to its corresponding electrode is ideally needed for efficient charge transport.

Once the charges reach the interface to the electrode the last step is the charge extraction. Interlayers are commonly placed between the photoactive layer and the electrodes to promote ohmic contact formation and to minimize series resistance and charge recombination.[41] Also, as will be described in section 2.4,

the donor and acceptor materials in the photoactive layer are often distributed in such a way that both materials would be in direct contact with both electrodes if no interlayers were present. Therefore, the interlayers also serve as charge selective layers that prevent the charges from exiting the photoactive layer through the wrong electrode.

## 2.3 Device characterization

### 2.3.1 Current-voltage characteristic

The energy band conditions of an organic donor/acceptor heterojunction sandwiched between two electrodes in darkness is shown in Figure 2.3.1 under different bias situations.

Under reverse bias (Figure 2.3.1a) electrons trying to enter the active layer from the anode (and holes trying to enter from the cathode) will experience a barrier that hinders the charge injection. Hence, in darkness only a very small current will flow under reverse bias.

Without any applied bias, i.e. at short circuit conditions, the HOMO and LUMO will still be tilted the same way as under reverse bias because of the built in electric field due to the different work functions of the electrodes, but not tilted as much. With increasing forward bias, the bands tilt less and eventually start tilting in the opposite direction. As this happens, electrons will be able to enter the active layer from the cathode and holes can enter from the anode and a much larger current can flow through the device than under reverse bias. In other words, the device has rectifying properties and will work as a diode in the dark. Figure 2.3.1d shows current as a function of applied bias (known as a J-V curve) for a solar cell in darkness; this current is called the *dark current*.

As previously described in section 2.2, if light is absorbed by the active layer, an exciton can be created and subsequently separated into free charges. If the device is under reverse bias, these free charges will experience a strong electric field and the device works as a photodetector. As the applied bias voltage changes from negative to positive and the fourth quadrant of the J-V diagram is entered (see Figure 2.3.2), there is still an internal electric field present due to the work function difference of the electrodes and the photocurrent flows in the same direction as before, but the dark current increases and flows in the opposite direction to the photocurrent. Thus, as the forward bias voltage increases the dark current increases and the total current decreases (Figure 2.3.2).

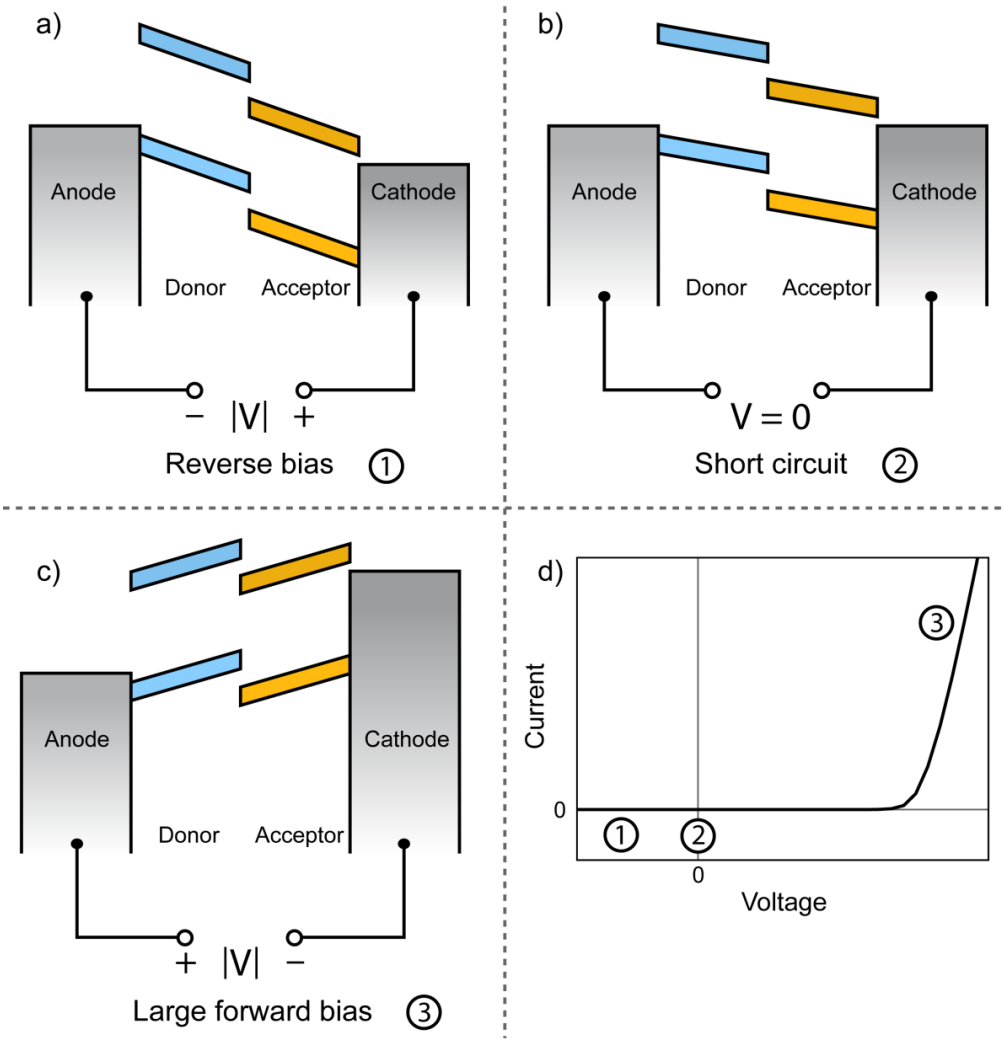


**Figure 2.3.1.** Energy band diagrams under different bias voltage conditions. Under reverse bias (a) the applied electric field tilts the bands, but due to the large energy barriers very few electrons are injected from the anode and very few holes are injected from the cathode and only a very small current can flow across the device. Under short circuit conditions (b) the bands are still tilted due to the built-in electric field. Under sufficiently high forward bias, the bands tilt the opposite way and electrons can be injected from the cathode and holes from the anode and a current can now flow across the device. (d) Dark current as a function of applied bias voltage.

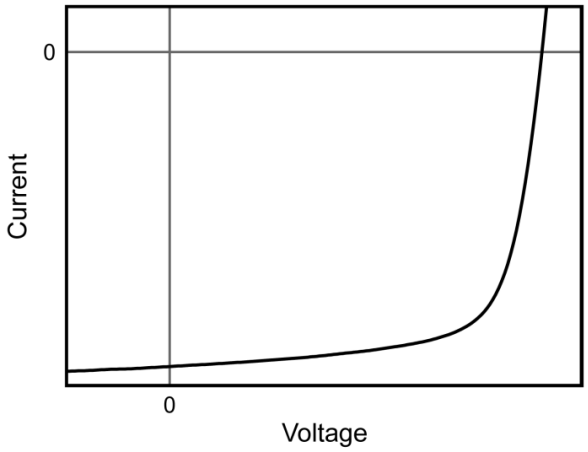


**Figure 2.3.2.** Solar cell current-voltage characteristics under illumination.

The current-voltage characteristics of a solar cell can be modelled as a current generator in parallel with a diode. A variety of processes that modify the current and voltage output can be taken into account by resistances added in parallel, $R_p$, and in series, $R_s$.[42] Figure 2.3.3 shows the equivalent circuit of a solar cell.

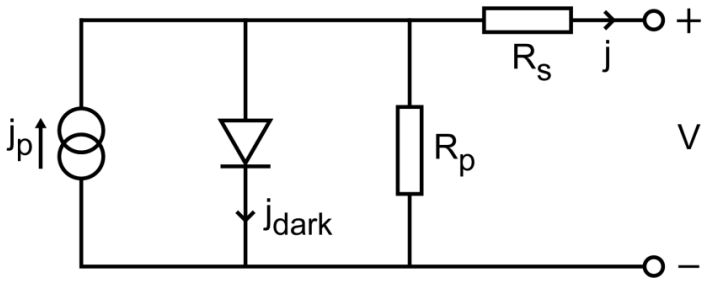


**Figure 2.3.3.** Solar cell equivalent circuit.

The diode can be modelled by the Shockley diode equation[43]

$$j_D = j_0 \cdot \left[ \exp\left( \frac{eV_D}{nk_BT} \right) - 1 \right] \tag{2.1}$$

where $j_D$ is the current density through the diode, $j_0$ the reverse bias saturation current density of the diode, e the elementary charge, $V_D$ the voltage across the diode, $n$ the ideality factor, $k_B$ Boltzmann's constant and $T$ the absolute

temperature. The current output $j$ from the solar cell under illumination as a function of applied voltage $V$ can then be written as

$$j = j_0 \cdot \exp\left[\left(\frac{e(V - jR_s)}{nk_BT}\right) - 1\right] + \frac{V - jR_s}{R_p} - j_p \qquad (2.2)$$

In equation (2.2) above, the photocurrent $j_p$ is assumed to be constant, even though, strictly speaking it is not entirely constant, but is nevertheless often a good approximation.[44]

The performance of a solar cell is evaluated from an experimentally measured current-voltage characteristic curve. Figure 2.3.4 shows a J-V curve of a solar cell under illumination where several important solar cell parameters are highlighted as well as a power-voltage curve.

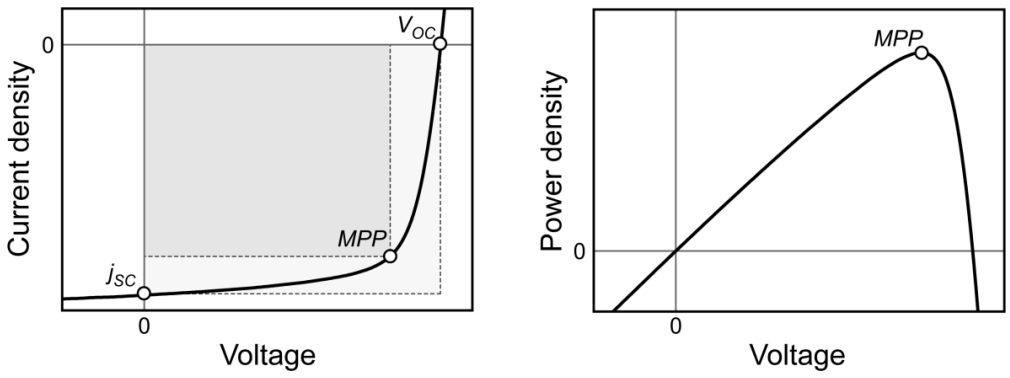


**Figure 2.3.4.** Solar cell J-V characteristics under illumination (left). Power density (right)

The current density that flows through the solar cell when no voltage is applied, or equivalently, when the resistance of the external load is zero, is called the *short circuit current density* ($J_{SC}$). There are several factors that influence the $J_{SC}$, such as the intensity and spectrum of the incoming light, the absorption coefficients of the materials in the active layer, as well as the efficiency of the exciton dissociation, charge transport and charge extraction.

The voltage where the photocurrent and the dark current are equal and cancel out so that the total current through the device is zero is called the *open circuit voltage* ($V_{OC}$). Equivalently, this is the voltage that develops between the

electrodes under illumination when they are not electrically connected, hence its name. The $V_{OC}$ depends on the materials combination in the active layer and is linked to the energy difference between the LUMO of the acceptor and the HOMO of the donor.[42] Using [6,6]-phenyl-$C_{61}$-butyric acid methyl ester (PCBM) as the acceptor material, the following empirical relation was obtained for a number of different conjugated polymers as donors[45]

$$V_{OC} = \frac{\left|E_{HOMO}^{Donor}\right| - \left|E_{LUMO}^{PCBM}\right|}{e} - 0.3 \text{ V} \tag{2.3}$$

Using high band gap materials can thus result in a high $V_{OC}$. However, since high band gap materials also absorb a smaller part of the solar spectrum, the $J_{SC}$ would be lower than for low band gap materials. Therefore, the effect of the band gap on both the $V_{OC}$ and the $J_{SC}$ needs to be taken into account when choosing the solar cell materials.

The power density *P* generated from a solar cell is given by

$$P = jV \tag{2.4}$$

Different loads correspond to different points along the J-V curve, and the point $(V_{max}, j_{max})$ where the solar cell generates the most power is called the *maximum power point* (*MPP*), (see the right hand side of Figure 2.3.4).

The *fill factor* (FF) is defined as the ratio

$$FF = \frac{j_{\max} \cdot V_{\max}}{j_{SC} \cdot V_{OC}} \tag{2.5}$$

and gives a measure of how easily photogenerated charge carriers are extracted from the solar cell. Since $j_{\max} \cdot V_{\max}$ is equal to the area of the largest rectangle that will fit inside the J-V curve and the coordinate axes (see Figure 2.3.4), the FF can be visualized as the 'squareness' of the J-V curve; the more square shaped the J-V curve is, the closer the FF is to unity. The FF is strongly affected by parasitic resistances, and also depends on interface recombination and the balance between electron and hole mobilities.[46]

The *power conversion efficiency* (PCE) of a solar cell is defined as the ratio between the maximal generated power and the power of the incident light, $P_{in}$.

$$PCE = \frac{j_{\max} \cdot V_{\max}}{P_{in}} = \frac{FF \cdot j_{SC} \cdot V_{OC}}{P_{in}} \tag{2.6}$$

Thus, for an efficient solar cell the FF, $j_{SC}$ and $V_{OC}$ all should be as high as possible.

Since the intensity and spectrum of the incident light can affect many of the aforementioned photovoltaic parameters, it is important to have clearly defined illumination conditions for any given J-V measurement. Commonly used is the *Air Mass 1.5* (AM1.5) solar spectrum.[44] The AM1.5 global spectrum (shown in Figure 2.3.5) corresponds to sunlight attenuated by passing through the atmosphere at an angle of 48° from zenith, equivalent to passing through 1.5 times the length of atmosphere compared to from zenith. For convenience, the intensity of the AM1.5 spectrum is normalized so that the integrated irradiance is 1000 W/m$^2$.

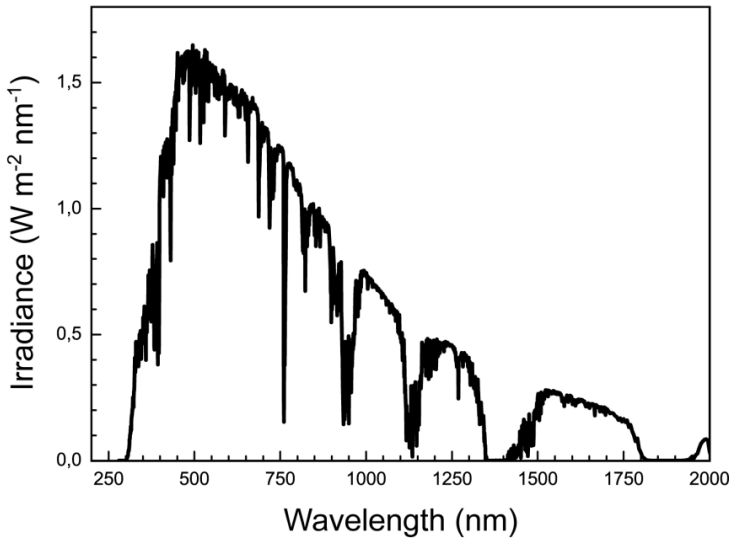


**Figure 2.3.5.** AM1.5 solar spectrum.[47]

### 2.3.2 Quantum efficiency

The current generated by a solar cell depends on the wavelengths of the incident light. How the different parts of the solar spectrum contribute to the total photocurrent is determined by measuring the quantum efficiency of the solar cell. The quantum efficiency is the probability that a photon with a particular energy will deliver an electron to the external circuit. A distinction is made between external quantum efficiency (EQE) and internal quantum efficiency (IQE). The EQE is given by the ratio between the number of electrons collected as photocurrent and the number of incident photons (equation 2.7), whereas the IQE relates the number of electrons collected as photocurrent to the number of absorbed photons (equation 2.8).

$$EQE = \frac{\text{number of electrons}}{\text{number of incident photons}} \tag{2.7}$$

$$IQE = \frac{\text{number of electrons}}{\text{number of absorbed photons}} \tag{2.8}$$

Since the EQE at any given wavelength gives the probability that a photon ultimately will contribute to the photocurrent, it is dependent on the efficiencies for photon absorption, exciton generation, exciton diffusion to a donor/acceptor interface, exciton dissociation and charge collection.

When measuring the EQE, the solar cell is illuminated by monochromatic light whose wavelength is varied while the current is measured, typically under short circuit conditions. Such a measurement results in a photocurrent spectrum that shows which wavelength regions contribute efficiently to the photocurrent. Usually a xenon lamp together with a monochromator is used as the light source, which means that the illumination intensity at every wavelength would be significantly smaller than the standard 1 sun intensity. This would then lead to a low current density in the device which may not be representative for the normal operating conditions for the solar cell at 1 sun intensity. For solar cells in which the $J_{SC}$ has a non-linear dependence on the illumination intensity, the EQE is also intensity dependent.[48] Therefore, in order to obtain more realistic operating conditions during EQE measurements, an additional white light source is often used to illuminate the device at 1 sun, a technique known as white light-biasing, or white light-soaking. The photocurrent generated by the monochromatic light is distinguished from that generated by the white light by

sending the monochromatic light through an optical chopper before it hits the solar cell. The frequency of the chopper is referenced to a lock-in amplifier, which enables the current generated by the monochromatic light to be measured separately.[49] The experimental setup is summarized below in Figure 2.3.6.

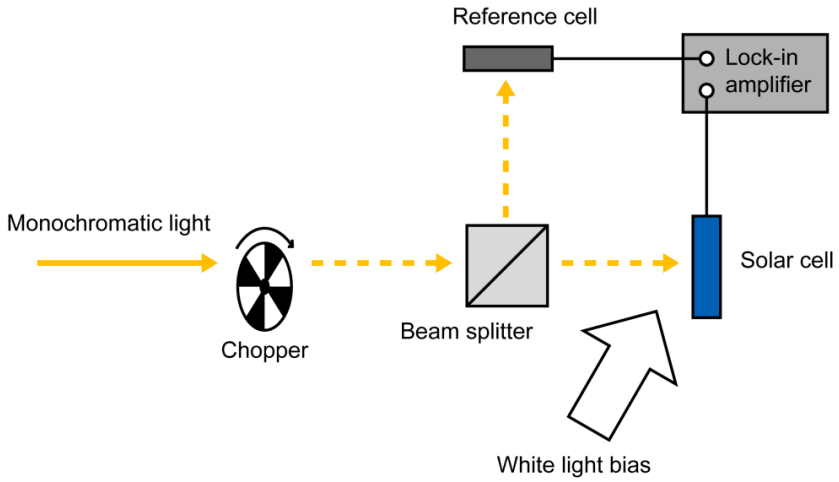


**Figure 2.3.6** Typical experimental setup for an EQE measurement system. The solar cell is illuminated by monochromated light passing through an optical chopper and simultaneously also by white light, typically at 1 sun intensity. Using a lock-in amplifier, the current generated by the monochromatic light can be measured separately. The wavelength of the monochromatic light is then varied as the EQE spectrum is recorded.

The EQE is routinely used as a control to check the reliability of the $J_{SC}$ values obtained from J-V measurements, and can help avoid errors due to e.g. incorrectly calibrated light intensity or inaccurate active area.[50] The $J_{SC}$ can be calculated by integrating the EQE together with the incident photon flux Φ(E),

$$J_{SC} = e\int EQE(E)\cdot\Phi(E)\,dE \qquad (2.9)$$

## 2.4 Morphology

How the donor and acceptor materials are distributed within the active layer of an organic solar cell is of great importance for the device performance.[16, 51-54] The first successful organic solar cell, reported by Tang et al. in 1986 had an active layer that was a bilayer of copper phthalocyanine and a perylene tetracarboxylic derivative.[55] As previously mentioned in section 2.2, only excitons that are generated close enough to a donor/acceptor interface to reach it by diffusion will contribute to the photocurrent. Therefore, a bilayer should not be thicker than twice the exciton diffusion length in order to avoid exciton recombination. Since the exciton diffusion length in organic semiconductors is in the range of 5-20 nm, this means that the bilayer then would be too thin to efficiently absorb light.

In 1995 the concept of the bulk heterojunction was introduced, in which the donor and acceptor materials are mixed within the same layer.[56, 57] Figure 2.4.1 shows typical bilayer and bulk heterojunction morphologies.

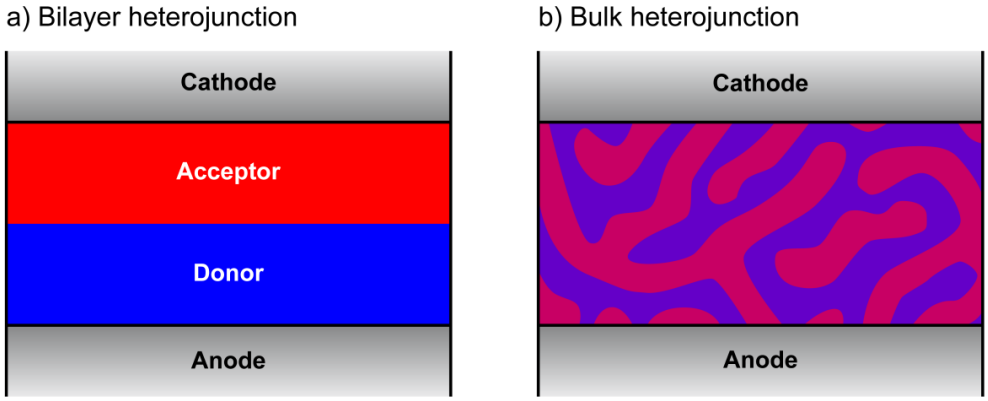


**Figure 2.4.1.** Illustration of typical bilayer (a) and bulk heterojunction (b) morphologies.

Compared to the bilayer heterojunction, the bulk heterojunction has significantly more interfacial area between the donor and acceptor materials and the interfaces are distributed throughout the film. Consequently, excitons can be efficiently dissociated in a larger fraction of the active layer even if the film is thicker than twice the exciton diffusion length. On the other hand, since the electrons are mainly transported through the acceptor material and the holes

through the donor material, efficient charge transport requires that once the exciton has been dissociated there exists continuous pathways of both donor and acceptor materials to the respective electrode. If the materials are too intimately mixed, there will be plenty of dead ends and bottlenecks that prevent the charges from easily reaching the electrodes. Considering this, the bulk heterojunction and the bilayer heterojunction excel at different aspects; in the bulk heterojunction the exciton dissociation is efficient whereas in the bilayer heterojunction the charge transport is efficient. However, comparing the device performance of the two, it is the bulk heterojunction that to date is the superior one.

For solution-processed materials, a bulk heterojunction is relatively simple to obtain through a one-step process in which the donor and acceptor materials are dissolved in the same solvent and mixed with each other before being coated onto a substrate. There are many ways to vary the morphology of the bulk heterojunction such as through the choice of solvent, annealing, materials combination, blend ratios, type of substrate, and deposition method.[51, 58-65] For vacuum-processed films, bulk heterojunctions can be obtained by co-evaporation.

Before the film is formed, when both materials are still in solution they form a homogenous mixture, but as the solvent evaporates the donor and acceptor materials will interact and generally start to phase separate into domains which are rich in either of the components. The extent of the phase separation will for a given materials combination depend on the film formation process. If the film dries slowly there will be sufficient time for the phases to form large domains, but if the drying is quick the system can be quenched into an intermediate state where the domains have not yet had the time to grow large before the structure is frozen in. This can be seen when comparing the morphologies of quickly drying spincoated films to more slowly drying drop cast films where the drop cast films exhibit larger domains.[65] The phase separation can later be reactivated by thermal annealing or solvent annealing.

The choice of solvent often has an effect on the morphology, not only because of the different drying time due to the difference in solvent vapor pressure, but also because of the solubility of the donor and acceptor materials in the solvents. If the solubility limit is lower in one solvent compared to another, the

phase separation will start earlier, giving more time for the phase separation and resulting in larger domain sizes.

In the early stages of the film formation, driven by differences in surface energy, the component that has the lowest surface energy will tend to move towards the free surface in order to minimize the total energy. As a result, a wetting layer rich in one of the components is commonly formed at the free surface.[66-72] Depending on how strongly the components interact and how much time they are given before the film is dry, interfacial instabilities may break up this layered structure into lateral domains,[73] see Figure 2.4.2.

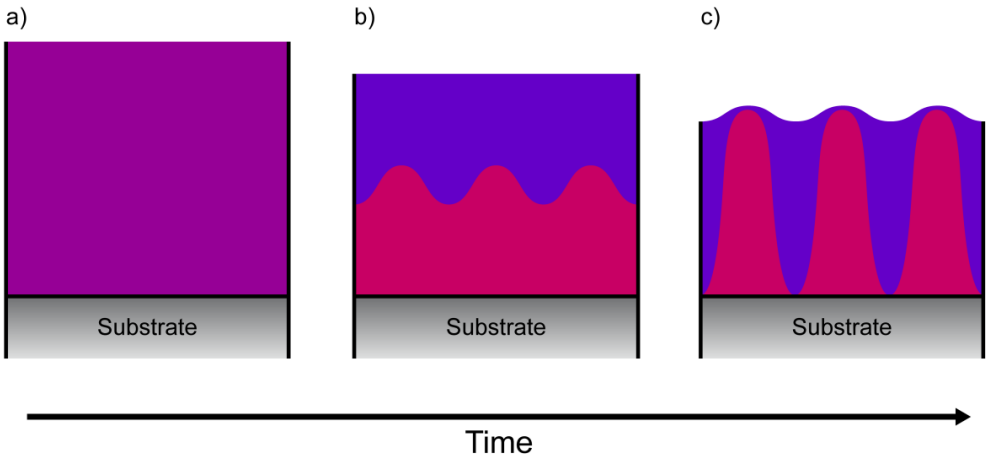


**Figure 2.4.2.** Schematic model illustrating morphology formation during drying. Starting from a homogeneous mixture (a), as the film dries, phase separation starts and initially creates a double layer due to surface energy differences (b). The layered structure can either be frozen in or develop further into a lateral structure (c).

Because of the impact morphology has on the performance of organic solar cells, it is of great importance to have proper tools for characterization. Structural as well as chemical information can be readily acquired via various microscopic and spectroscopic methods. A selection of experimental methods that can be used to probe the morphology is treated in more detail in chapter 4.

## 2.5 Stability

As the efficiencies of polymer solar cells have steadily improved over the last years, we are now reaching a point where stability rather than efficiency is becoming one of the major impediments for commercialization. In order to achieve higher stability, the degradation processes in the materials have to be understood. There are a number of external factors that can contribute to the degradation, such as water, oxygen, light and heat. Additionally, polymer solar cells degrade via several chemical and physical pathways that affect different parts of the device; the donor and acceptor materials, the active layer morphology, as well as the interlayers and electrode materials.[74-80] Thus, encapsulating the devices to protect them from the ambient atmosphere is necessary for long-term stability. Recently, large area (100 $cm^2$) modules, encapsulated using a simple low-cost packaging barrier, successfully maintained over 80% of the initial efficiency after more than 2 years of outdoor operation.[20]

The loss in solar cell performance differs depending on the type of degradation that has taken place. Observing changes to the JV-characteristics is a common way to monitor the progression of the degradation, and how to the different photovoltaic parameters are affected can provide valuable insight into the nature of the degradation. The $J_{SC}$ is directly related to light absorption, exciton dissociation, charge transport and charge extraction at the electrodes. Consequently, if one or more of those steps are impaired by the degradation, the $J_{SC}$ would decrease. A decrease in $V_{OC}$ could be due to e.g. changes to the electronic structure of the donor and acceptor materials or the work function of the electrodes.[81, 82] Degradation that either increases the series resistance or decreases the parallel resistance would lead to a reduced FF, as would any processes that increase interface recombination or disturb the balance between electron and hole mobilities.[46, 81]

Low work function metals such as aluminium and calcium are commonly used for top electrodes in polymer solar cells. Such metals are highly reactive to oxidation and form oxides with insulating properties, thus forming barriers to charge extraction.[83] It has been suggested that water can diffuse through pores in the metal layer and form metal oxides at the interface between the electrode and the rest of the device.[74] It has also been shown, using secondary ion mass spectrometry that oxygen from the surrounding atmosphere can diffuse

through grain boundaries and microscopic holes in the aluminium electrode and into the device.[78, 84]

LiF is commonly used as an interlayer between the active layer and the top electrode and can improve the fill factor and $V_{OC}$.[85] Kawano et al showed that LiF also could improve the device stability of P3HT:PCBM solar cells during the first 8 hours of illumination.[86] However, thin layers of LiF have also been shown to decompose during the deposition of the aluminium top contact.[87]

Poly(3,4-ethylenedioxythiophene) polystyrene sulfonate (PEDOT:PSS) is currently one of the most common materials used as a hole transport layer. However, due to its acidic nature with pH as low as 1-3,[74] it can together with water corrode the adjacent electrode; especially those made from metals but also ITO has been shown to etch in the presence of PEDOT:PSS.[76] PEDOT:PSS is found as one of the main sources of device degradation. Alternative hole transport layers are therefore widely investigated.

When conjugated polymers are photo-oxidized they tend to bleach as the loss in conjugation destroys the chromophores,[75] leading to reduced light absorption. By comparing the UV-Vis spectra of films of poly[2,3-bis-(3-octyloxyphenyl)quinoxaline-5,8-diyl-alt-thiophene-2,5-diyl] (TQ1) of different molecular weights to degraded films, Henriksson et al. assigned the bleaching to chain scission due to photo-induced oxidation.[88] Reese et al. have shown that the photobleaching of poly(3-hexylthiophene) (P3HT) blended with PCBM is much slower than that of pristine P3HT and rationalized this by a process where PCBM quenches the photoexcited state of the polymer, hence protecting it from photo-oxidation.[79] Apart from photochemical reactions, oxygen can also p-dope the active layer, forming a space charge region in front of the cathode that shields the electric field and hinders charge extraction.[89]

Manceau et al. investigated the photochemical stability of 24 different conjugated polymers using UV-Vis and infrared spectroscopy and were able to find some general rules connecting the chemical structure to stability. Several common monomers were ranked by their degree of stability. Fluorene units were shown to be far less stable than e.g. thiophene units. It was also found that the position and number of side chains affected the stability; with high numbers of sidechains leading to low stability.[90] Hoke et al. investigated the photobleaching of polymer:fullerene blends in the presence of oxygen and

found the degradation to depend on the position of the fullerene's LUMO. With decreasing electron affinity, the rate of photobleaching of the blend increased, and a mechanism was proposed where electron transfer from the polymer or fullerene to diatomic oxygen generates oxygen radicals that degrade the polymer.[91]

As mentioned in section 2.4, the active layer typically forms a metastable blend of the donor and acceptor materials. During illumination, the active layer may reach temperatures high enough to initiate further phase separation,[92] leading to larger domains, with less effective exciton dissociation and a smaller photocurrent as a possible result. High temperature can also trigger the growth of large, micrometer sized PCBM crystals[93-96] that will hamper the solar cell performance considerably.

While most work on the degradation of the active layer has been focused on the polymers, PCBM has also been shown to degrade when exposed to light and air. Reese et al. observed oxidation of PCBM after exposing a P3HT:PCBM blend film to light in ambient air for 1000 hours.[79] It has also been shown by Chambon et al. that the photo-oxidation of PCBM mainly involves the oxidation of the $C_{60}$ moiety.[97] Anselmo et al. recently used near-edge X-ray absorption fine structure (NEXAFS) and X-ray photoelectron spectroscopy (XPS) to study the effect of light exposure in air on the electronic structure of PCBM, they found distinct changes to both the occupied and unoccupied molecular states already after 30 minutes of exposure.[98] The influence of ambient atmosphere on PCBM has been investigated by Bao et al. who exposed PCBM films to oxygen gas and water vapour in darkness. Changes to the PCBM work function were observed after water vapour exposure, and the valence band spectrum was also strongly affected by the exposure to water vapour.[99]

### 2.5.1 Encapsulation

Given the sensitivity of polymer solar cells to photo-degradation in the presence of oxygen and moisture, the importance of protection from the ambient atmosphere is evident. Encapsulating the solar cell using suitable materials can provide this protection. Apart from forming a barrier for oxygen and water, the encapsulation material also needs to have a high transparency, at least on one side of the solar cell. Moreover, in order to achieve the low-cost production of polymer solar cells, the cost of encapsulation cannot be too high.

A readily available material with excellent barrier properties against oxygen and water is glass. It is common for polymer solar cells produced on the laboratory scale to be processed on glass substrates, so the device can be encapsulated in a relatively straightforward manner by placing a glass slide on top. The two glass sheets are usually sealed together by an adhesive such as UV-curable or thermosetting epoxy resins. Since the glass itself is practically impermeable to oxygen and water, it is the edge sealing that forms the weakest part of the encapsulation.[100] In 2006 Krebs encapsulated a P3HT:PCBM solar cell between a sheet of glass and a thick aluminium back plate and demonstrated an operational stability of more than one year in which time 65 % of the initial efficiency was retained.[101] An obvious problem with glass as the encapsulation material is, however, that the mechanical flexibility of the polymer solar cell is sacrificed. For laboratory use, on the other hand, this type of encapsulation is a convenient technique.

Using mechanically flexible materials to keep water and oxygen away is something that is well known in the food and pharmaceutical packaging industry. Commonly available, low-cost polymers are too permeable to oxygen and water to be used on their own in the packaging of sensitive products.[102] This led to the development of barrier films that are integrated with the plastic film. A common example of this is an aluminium layer, a few tens of nanometers thick, deposited onto a polymer film. Such a structure can improve the barrier properties by two orders of magnitude with respect to the bare polymer film.[103] For solar cells, however it is important that light can pass through the encapsulation, hence the use of metals as barrier films is not ideal. Thin oxide films, such as $SiO_x$, have also been used successfully on polymer substrates, offering good barrier properties while retaining optical transparency, mechanical flexibility and cost-effectiveness.[102]

### 2.5.2 Concentrated light

As the life times of polymer solar cells increase, now displaying operational stability exceeding two years,[20] stability testing under normal operating conditions is becoming increasingly time-consuming. For this reason, techniques for accelerated aging can be useful in order to obtain stability information within a more convenient timeframe. Accelerated aging can be realized by changing the temperature or the atmosphere.[74, 104, 105] For photo-degradation studies, concentrated light can also be used, and is a promising tool to accelerate the degradation processes.[100]

Normally the light used in most concentrator setups is sunlight, even though simulated sunlight also can be used.[106] In order to control environmental factors such as ambient temperature and atmosphere, it is often not desirable to conduct the degradation experiments outdoors. When using concentrated sunlight for degradation studies, it is therefore common to focus the light onto an optical fiber that allows the concentrated light to be guided indoor where the environment can be controlled.[107]

Tromholt et al. used a lens-based solar concentrator to accelerate the degradation of conjugated polymers. The material degradation was monitored by UV-Vis and infrared spectroscopy and compared for different solar concentrations. The polymers were found to degrade much faster under concentrated sunlight, and a degradation acceleration factor was deduced from the rates of photo-bleaching under different illumination intensities. The acceleration factor was found to depend linearly on the intensity of the concentrated sunlight. Infrared spectroscopy further revealed that the modifications to the polymer due to exposure to concentrated sunlight were similar to those caused by exposure to 1 sun. Hence, concentrated sunlight can allow otherwise time-consuming degradation studies to be performed within a much shorter time without having the degradation mechanisms significantly altered.[108]

A problem that can be encountered when using concentrated sunlight to accelerate the photo-degradation is that the high intensity light will heat the sample much more than under normal sunlight. Madsen et al. studied the degradation of P3HT and found the increase in photo-bleaching with increased illumination dose to be similar for different light concentrations as long as the samples were cooled to keep a constant temperature. Without cooling of the samples on the other hand, the photo-bleaching increased faster with

illumination dose for concentrated light than for lower intensity light.[106] Thus, when using concentrated light it is important to separate the light-induced degradation from any potential thermally induced degradation. Visoly-Fischer et al. demonstrated accelerated degradation of P3HT:PCBM solar cells using concentrated sunlight while maintaining the solar cells at low temperature. This was achieved by chopping the light, thus allowing heat accumulated during the illumination to be dissipated during the non-illuminated period.[109]

## 2.6 Hole transporting layers

As was described in section 2.4, the morphology of the active layer in polymer solar cells is often such that the donor and acceptor materials are in direct contact with both electrodes. For this reason, interfacial layers are commonly placed between the active layer and the electrodes in order to improve charge selectivity and enhance charge extraction.[41] The layer placed between the active layer and the anode is known as the hole transporting layer (HTL) whereas that placed between the active layer and the cathode is known as the electron transporting layer. Here the main focus will be placed on HTLs.

In order to function as an efficient HTL, an interfacial layer should have a number of properties. First of all, its work function should be high enough to match the HOMO of the donor. This way, a high contact barrier at the anode/donor interface can be avoided and ohmic contact between the anode and the active layer is promoted. If the conduction band of the HTL material lies sufficiently far above the LUMO of the active layer materials, the HTL will also prevent electron transfer into the anode. Figure 2.6.1 shows the energy level diagram of the components of an organic solar cell with an HTL material that has an electronic structure such that hole collection by the anode is facilitated while electron transport to the anode is blocked.

Since it is only the light that reaches the active layer and is absorbed that will generate excitons and thus contribute to the photocurrent, the optical properties of the HTL are important. The HTL should have a high transmittance in the spectral region where the solar cell operates. Materials with high band gaps are therefore suitable since they have high optical transmittance in most of the solar spectrum. In solar cells with the conventional device structure (as shown in Figure 2.2.1) where the active layer is deposited on top of the HTL, the HTL material should also have a surface energy that allows for good wetting and film formation of the active layer. Materials used as HTLs should also have a high hole mobility.

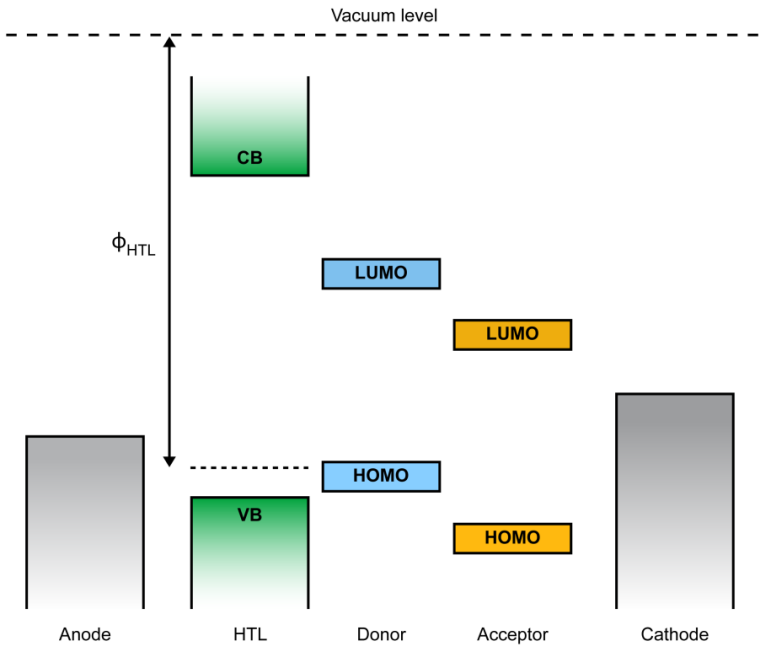


**Figure 2.6.1.** Energy level diagram of the components of an organic solar cell with a wide band gap, p-type semiconductor as an HTL. The HTL should have a high work function in order to match the HOMO of the donor material, allowing ohmic contact to be formed. Additionally, if the conduction band energy of the HTL is low enough, transfer of electrons to the anode is blocked.

Several different types of materials have successfully been used as HTLs in polymer solar cells. One of the most commonly used is PEDOT:PSS, a water-soluble polyelectrolyte that can have a high electrical conductivity and exhibits a high optical transparency in the visible region.[110, 111] The relatively high work function of PEDOT:PSS can lead to a low energy barrier for holes at the interface between the active layer and the PEDOT:PSS.[112, 113] However, the major drawback of PEDOT:PSS lies in its adverse chemical properties such as its hygroscopic and acidic nature, which have been shown to be detrimental for the long term stability of BHJ organic solar cells.[74, 75, 77, 114] Also, many of the recent state-of-the-art donor materials are designed to have a deep-lying HOMO in order to maximize the $V_{OC}$,[115] therefore having HTLs with high work functions has become increasingly important. The work function of PEDOT:PSS, although exhibiting some spread depending on formulation and processing conditions,[116, 117] tends to be too low to match the deep-lying HOMO of many of the newer donor materials. By using high work function metal oxides as HTLs instead of PEDOT:PSS, these drawbacks can be overcome.

There are several different high work function metal oxides that have been successfully used as HTLs, including $NiO_x$, $MoO_3$, $V_2O_5$, and $WO_3$.[118-121] Among these metal oxides, $NiO_x$ is the only p-type material while the others are all n-type.[120-123] At first it was believed that $MoO_3$, $V_2O_5$, and $WO_3$ also were p-type, but later studies showed, using a combination of ultraviolet photoelectron spectroscopy (UPS) and inverse photoemission spectroscopy, that they are n-type materials with very deep lying electronic states.[121, 124, 125]

While pure, stoichiometric NiO is an insulator,[126, 127] non-stoichiometric $NiO_x$ is a p-type, wide band gap semiconductor.[122, 128-131] $NiO_x$ has a high optical transmittance in the visible region, a valence band energy that is close to the HOMO of many donor materials, allowing transport of holes to the anode while the high conduction band energy prevents electrons from reaching the anode so that recombination at the interface is avoided.[122, 131-133] $NiO_x$ has been used as the HTL in organic solar cells, deposited by several different methods such as pulsed-laser deposition,[122, 134] thermal evaporation,[135] atomic layer deposition,[136, 137] sputtering[138, 139] and solution processing,[131-133, 140-143] often outperforming their PEDOT:PSS-based counterparts. Of all these aforementioned deposition techniques, solution processing is the one that is most suitable for low cost, large scale fabrication of organic solar cells due to the compatibility with roll-to-roll printing and the fact that no vacuum is required.

Solution processed $NiO_x$ films are usually made from a precursor solution containing nickel formate,[141, 144] nickel acetate[133, 142, 143, 145] or nickel chloride[146]. After depositing a thin layer of the precursor solution, thermal annealing can then convert the precursor into $NiO_x$.[131-133, 141, 144] To increase the work function of the $NiO_x$ HTL, exposure to oxygen-plasma[131, 134, 139, 144] and UV-ozone[142, 143] has been used successfully.

# Chapter 3
# Materials and sample preparation

## 3.1 TQ1

The main polymer studied in this thesis is poly[2,3-bis-(3-octyloxyphenyl) quinoxaline-5,8-diyl-alt-thiophene-2,5-diyl] (TQ1). TQ1 is an alternating copolymer that consists of thiophene and quinoxaline units. To make the polymer soluble in common organic solvents, two octyloxyphenyl side groups are attached to the quinoxaline unit. The molecular structure is shown in Figure 3.1.1.

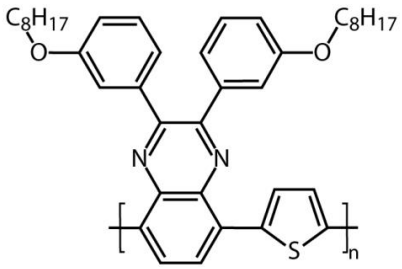


**Figure 3.1.1.** Molecular structure of TQ1.

TQ1 was first synthesized in 2003 by Yamamoto et al.[147] and used for the first time as the electron donor in solar cells in 2010 by Wang et al.[148] Used together with the fullerene derivative [6,6]-phenyl $C_{71}$-butyric acid methyl ester ($PC_{70}BM$), the solar cells initially displayed a PCE of up to 6%,[148] which was later pushed to 7% by morphology control using solvent additives.[149]

TQ1 belongs to a class of conjugated polymers called donor-acceptor polymers. By having units along the polymer backbone that are alternatingly strongly acceptor-like and strongly donor-like, the band gap of the polymer can be reduced.[150] In TQ1, the thiophene is the donor-like unit and the quinoxaline the acceptor-like unit. The optical bandgap of TQ1 is 1.7 eV.[148]

Being easy to synthesize[148] and also displaying a higher thermal and chemical stability than many other commonly used electron donating polymers such as P3HT,[151] TQ1 is a promising solar cell material for the future.

## 3.2 PCDTBT

Another polymer studied in this thesis as an electron donor is poly[N-(1-octylnonyl)-2,7-carbazole]-alt-5,5-[4',7'-di(thien-2-yl)-2',1',3'-benzothiadiazole] (PCDTBT). PCDTBT is an alternating copolymer that, just like TQ1, belongs to the class of donor-acceptor polymers, and consists of electron donating carbazole and electron accepting benzothiadiazole units that are bridged by thiophene units.[115] Alkyl chains are added to the carbazole units for improved solubility. The molecular structure of PCDTBT is shown in Figure 3.2.1.

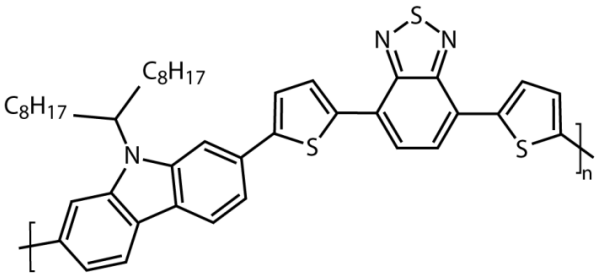


**Figure 3.2.1** Molecular structure of PCDTBT.

PCDTBT was first synthesized in 2007 by Blouin et al. The optical band gap is 1.88 eV and initial solar cells displayed an efficiency of 3.6 %,[152] which was later increased to above 7.2% by the combined use of $TiO_x$ as an optical spacer and $MoO_3$ as the HTL.[153]Additionally, PCDTBT-based solar cells have displayed a remarkably high IQE, close 100 % for light of around 450 nm wavelength, which means that almost every absorbed photon in that range generates free charge carriers that are able to reach the electrodes.[154]

Carbazole derivatives, which PCDTBT is an example of, have displayed good chemical and thermal stability as well as relatively high charge mobility,[152, 155] making them promising as solar cell materials. For example, even though carbazole is structurally very similar to fluorene, replacing the carbon atom on the central fluorene ring with nitrogen improves the chemical stability by preventing the ketone formation normally associated with the oxidation of fluorene which would be detrimental to the electronic and optical properties.[155]

## 3.3 Fullerene derivatives

For solar cell applications, some of the most commonly used electron acceptors are fullerene derivatives. Fullerenes themselves have good electron accepting properties due to their high electron affinity but, owing to their low solubility in most common solvents, are not ideal for solution-processed solar cells and are normally limited to devices produced by vacuum deposition. By adding a suitable functional group to the fullerene cage, however, the issue with low solubility can be resolved. The fullerene dervative [6,6]-phenyl-$C_{61}$-butyric acid methyl ester ($PC_{60}BM$) was synthesized in 1995 by Hummelen et al.[156] and is to date one of the most commonly used acceptor materials in polymer solar cells. The molecular structure of $PC_{60}BM$ is shown in Figure 3.3.1a.

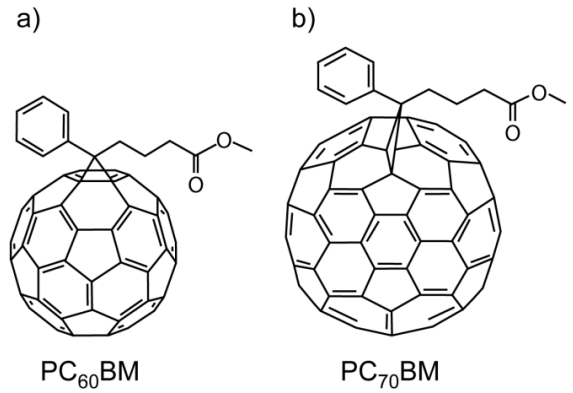


**Figure 3.3.1.** Molecular structure of a) $PC_{60}BM$ and b) $PC_{70}BM$.

Apart from being a good electron acceptor, fullerene derivatives also have relatively good electrical transport properties with an electron mobility on the order of $10^{-2}$ $cm^2/(V \cdot s)$ for $PC_{60}BM$.[157] Another widely used fullerene derivative is [6,6]-phenyl-$C_{71}$-butyric acid methyl ester ($PC_{70}BM$), that exhibits stronger light absorption in the visible range than $PC_{60}BM$.[158] The molecular structure of $PC_{70}BM$ is shown in Figure 3.3.1b.

## 3.3 Spin-coating

Spin-coating is a common technique used to produce thin film coatings on flat substrates. For polymer solar cell research it has found a particularly widespread use as it provides a quick and easy way to create uniform and thin (~100 nm) films. As the name might allude to, spin-coating works by placing a solution of the coating material on a substrate and subsequently spinning it until a dry film has formed. This process can be divided into the following sub-steps[159] that are illustrated schematically in Figure 3.3.1.

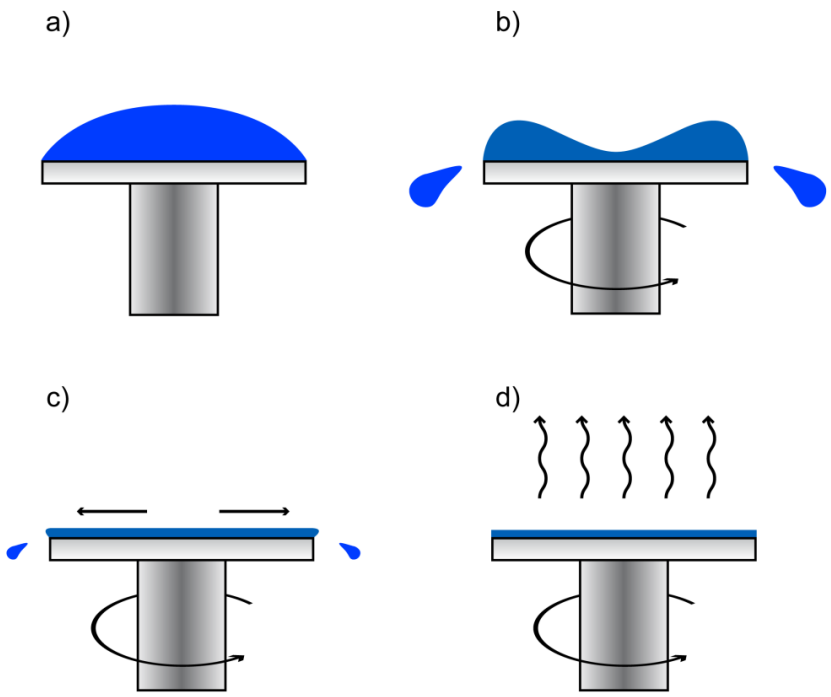


**Figure 3.3.1.** Schematic illustration of the spin-coating process. (a) The solution is dispensed. (b) The substrate is rotationally accelerated and excess solution thrown off. (c) Solution flows off the substrate, the flow decreasing as the solvent evaporates and the film viscosity increases. (d) As the flow ceases, fluid is only lost through solvent evaporation.

After an excess amount of solution has been dispensed (Figure 3.3.1a), the substrate is rotationally accelerated (Figure 3.3.1b). In this first step, about 90% of the solution is thrown off as the substrate starts spinning.[159] The initial amount of solution has little or no effect on the final film thickness.[160] The acceleration time until the final spin speed is reached does not affect the final

film thickness either, but can influence the radial uniformity of the film if long acceleration times are used.[161]

In the next step, the rotation makes the solution flow radially outward (Figure 3.3.1c), reducing the film thickness while at the same time solvent evaporation also increases the viscosity of the film. Since the flow is governed by the balance between centrifugal and viscous forces, the flow decreases as the concentration and thus the viscosity if the film increases. It is mainly during this step that phase separation occurs.[162]

The final step begins when the viscosity of the film has become high enough that the flow is negligible. From that point on, solvent evaporation is the dominant fluid loss (Figure 3.3.1d).

Several different factors influence the final film thickness during spin-coating. Since the final film thickness is mainly determined during step c) in Figure 3.3.1, high spin speeds lead to low final film thicknesses. High initial solution concentrations on the other hand give a high solution viscosity early in the process and consequently lead to thicker films. High vapour pressure solvents evaporate quickly so that the viscosity also increases quickly, also giving thicker films. An empirical relation between film thickness $d$ and spin speed $\omega$ is given by

$$d = k \cdot \omega^{\alpha} \tag{3.1}$$

where $k$ and $\alpha$ are empirically determined constants, dependent on solution properties and substrate. $\alpha$ typically has a value in the vicinity of -0.5.[160]

# Chapter 4
# Experimental techniques

## 4.1 Atomic force microscopy

Atomic force microscopy (AFM) is a scanning probe technique used to characterize surfaces, most notably the surface topography. First developed in 1986 by Binnig et al.[163] the AFM made high-resolution studies of surfaces of insulating materials possible. The scanning tunneling microscope (STM), developed a few years earlier,[164] relies on tunneling currents and is thus restricted to conducting or semiconducting samples. Both STM and AFM utilize a very sharp tip that is scanned across the sample surface; the STM detecting electron tunneling whereas AFM detects the forces between tip and sample. The resolution of AFM images can be very high, with atomic resolution having been demonstrated, both in vacuum[165] and on surfaces covered by liquids.[166]

The interactions between the tip and the sample can be approximated by the Lennard-Jones potential[167]

$$U = 4\varepsilon\left[\left(\frac{r_0}{r}\right)^{12} - \left(\frac{r_0}{r}\right)^{6}\right] \tag{4.1}$$

where $U$ is the interaction potential, $r$ the distance between the tip and the sample, $\varepsilon$ the depth of the potential and $r_0$ the finite distance where the potential is zero. The negative term in equation (4.1) is the attractive contribution from Van der Waals forces and the positive term is due to Pauli repulsion, i.e. from the overlap of electron orbitals. The Lennard-Jones potential is shown in Figure 4.1.1.

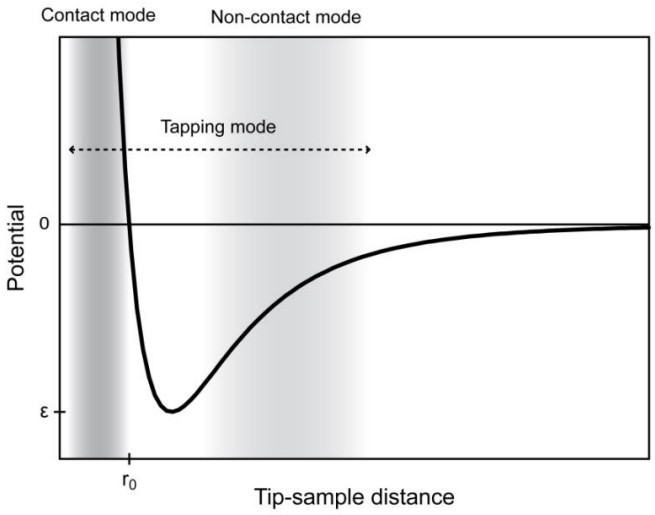


**Figure 4.1.1.** Lennard-Jones potential along with the operational ranges of contact mode, non-contact mode and tapping mode.

The instrumental setup of a typical AFM system is shown in Figure 4.1.2. The tip is mounted on a cantilever, allowing forces to be measured via the deflection of the cantilever. The deflection is measured by reflecting a laser beam from the top surface of the cantilever onto a position sensitive photodiode. The sample and the tip are moved relative to one another by a piezoelectric stage that can move in the x, y and z directions.

There are several different imaging modes for AFM; some of the more common ones being contact mode, non-contact mode and tapping mode.
Contact mode operates in the repulsive part of the interaction potential (see Figure 4.1.1). The tip is brought into contact with the sample and usually kept at a constant force as the tip is scanned across the sample. A feedback loop assures that the force is kept constant by moving the cantilever relative to the sample in the z-direction using the piezo crystal. That way, as the sample is scanned, at every point (x,y), the z-position is recorded and gives a three-dimensional image of the sample surface. As the forces between tip and sample can be relatively high in contact mode, hard samples are preferable. Soft samples can easily be damaged, especially by lateral forces as the tip is dragged across the sample surface. Also, the area of contact between the tip and the sample is higher for soft samples, thus limiting the resolution.[168]

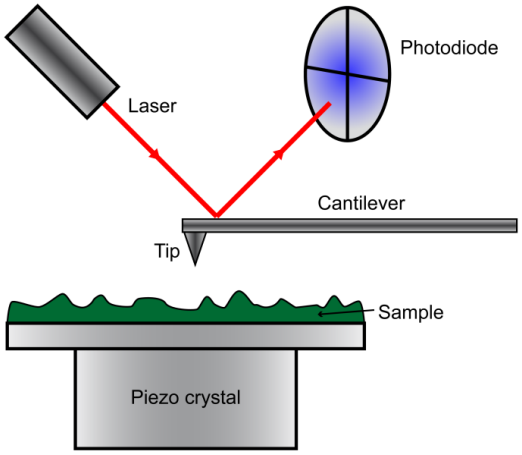


**Figure 4.1.2.** Typical AFM setup.

Non-contact mode operates further away from the sample in the attractive part of the interaction potential (see Figure 4.1.1). The tip is not in direct contact with the sample and the cantilever is made to oscillate near its resonance frequency. The interactions with the sample shift the frequency of the oscillation, and this frequency shift can be kept constant by the feedback loop by varying the z-position of the cantilever, thus mapping the sample topography. Here the forces between tip and sample are lower than in contact mode so sample damage from the tip is small, as is the area of contact between the tip and the sample, allowing for very high resolutions. However, when measuring in air, the sample surface may be covered by contaminant layers (e.g. water) thicker than the range of the attractive forces being probed.[168]

Tapping mode (also known as intermittent contact mode) operates within both the range of contact and non-contact mode. Just like in non-contact mode, the cantilever is made to oscillate, but now at much higher amplitude so that the tip once per oscillation is brought into contact with the sample, tapping it. Usually constant amplitude is maintained by the feedback loop while the sample is scanned. Apart from measuring the topography, the phase difference between the driving frequency and the actual oscillation frequency can also be recorded at every point. The phase difference is sensitive to the stiffness of the sample,[169] so it is possible to distinguish between materials of different stiffness in the phase image. Tapping mode avoids the damage to soft samples associated with contact mode, while also being able to operate in ambient air, since any layers of adsorbed water are easily penetrated by the tip.

## 4.2 Secondary ion mass spectrometry

Secondary ion mass spectrometry (SIMS) is a chemically sensitive analysis method based on ion sputtering. A beam of primary ions hits the sample surface, and upon impact ejects particles from the surface (Figure 4.2.1). These particles include ions, neutral atoms and molecules, as well as electrons and photons. In SIMS, these ejected secondary ions are sent to a mass spectrometer to be analysed. The mass spectrometer measures the mass-to-charge (m/q) ratio of the ions, thus giving information about the chemical composition of the sample. Since the secondary ions originate from very close to the surface (<1 nm), this technique gives surface sensitive chemical information.[170]

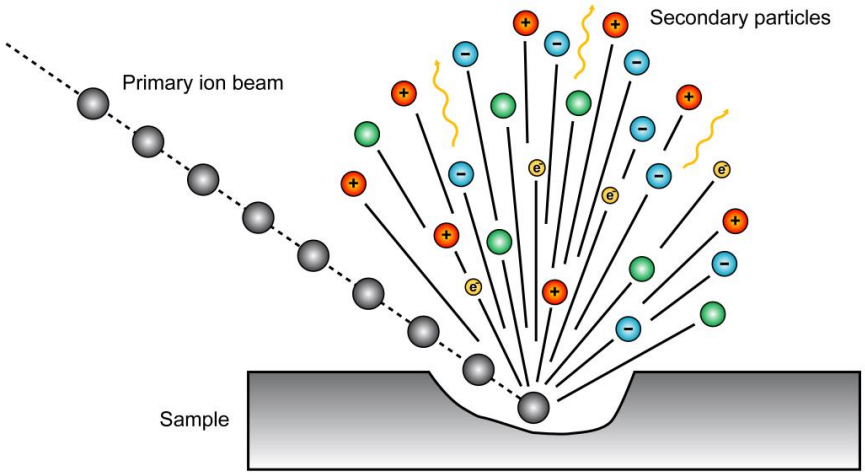


**Figure 4.2.1.** Illustration of the sputtering process in SIMS. Note though that in the figure, the relative amount of charged particles in relation to neutral ones is exaggerated; in a true situation only a small fraction of the secondary particles leave the surface charged.[170]

Sputtering using low primary ion doses to analyse the chemical composition of the topmost layer of the sample is known as static SIMS. By using higher doses, or a separate source of primary ions intended only to remove material, secondary ions can be collected throughout the sample. This mode, known as dynamic SIMS, produces depth profiles with vertically resolved compositional information. Furthermore, by scanning the primary beam laterally, composition maps can be obtained, and if used in combination with depth sputtering, complete three-dimensional maps can be created.

After the secondary ions have been generated, they are extracted and accelerated by an electric field. Because of the spread in kinetic energy from the sputtering process, the secondary ions are then sent through an energy filter before entering the mass spectrometer. There are several different types of mass spectrometers. A sector field mass spectrometer uses static electric or magnetic fields (or a combination of both) to separate ions of different m/q ratios. In a quadrupole mass spectrometer the secondary ions are sent along four parallel metal rods. Oscillating electric field are applied to the rods such that only ions having a specific m/q ratio can pass through. A time-of-flight mass spectrometer measures the time it takes the ions to travel a given distance. After being accelerated by an electric field and sent through an energy filter, ions having the same charge will also have the same kinetic energy, travelling at different speeds depending on the mass; thus allowing the m/q ratio to be obtained by measuring the time of flight. Time-of-flight mass spectrometers require that either the primary ion beam or the acceleration field is pulsed.

Although SIMS makes it possible to determine where in a sample certain chemical species are located, as well as how the concentration changes in space, the information is usually qualitative. Translating specific m/q intensities to absolute concentrations is difficult since the detection sensitivities for different elements vary.[170]

## 4.3 Synchrotron radiation

Since the discovery of X-rays in 1895 by Röntgen,[171] a considerable number of techniques have been developed that use X-rays to characterize materials. The first X-ray sources were X-ray tubes; vacuum tubes where electrons are accelerated by a high voltage and produce X-rays as they hit the anode. The maximum photon flux that can be produced by an X-ray tube is however limited by the heating of the anode caused by the decelerating electrons, even if this problem can be reduced by using water cooling and a rotating anode.[172] To get higher flux, synchrotrons are used. It is worth noting though, that the total photon flux from a light source is not the only factor determining how many photons ultimately will hit a sample and is therefore not the ideal quantity for comparing light sources. Brilliance (or brightness as it is also commonly referred to) is a measure related to the number of photons emitted per second per bandwidth per unit solid angle and unit area of the source.[173] Compared to X-ray tubes, the achievable brilliance of synchrotron radiation sources can be more than 14 orders of magnitude higher.[174]

It is well known that accelerated charges emit photons.[175] Synchrotron radiation is produced as the trajectory of electrons moving at relativistic speeds is bent; hence the radial acceleration of the electrons causes the emission of radiation. Since the electron velocity is very close to the speed of light, an observer looking at approaching electrons will see a large relativistic Doppler shift. The radiation is emitted along the tangent of the electron path in a narrow cone, with its divergence $\theta$ given by[174]

$$\theta \sim \gamma^{-1} \tag{4.2}$$

where $\gamma$ is the Lorentz factor. Since $\gamma$ typically is on the order of 1000 or more for most synchrotron facilities,[176] the divergence is usually less than a milliradian, which is part of the reason for the high brilliance of synchrotron radiation sources.

Figure 4.3.1 schematically depicts some of the main components of a synchrotron. Electrons are normally generated from a hot cathode by thermionic emission and accelerated first by a linear accelerator (linac) before being sent into a booster ring. In the booster ring the electrons are further accelerated before they are injected into the storage ring. Modern storage rings

are generally not completely circular, but rather shaped like a regular polygon. The electron beam is bent at the corners by dipole magnets, called *bending magnets*, which apart from just keeping the storage ring beam in a closed path also produce synchrotron radiation.

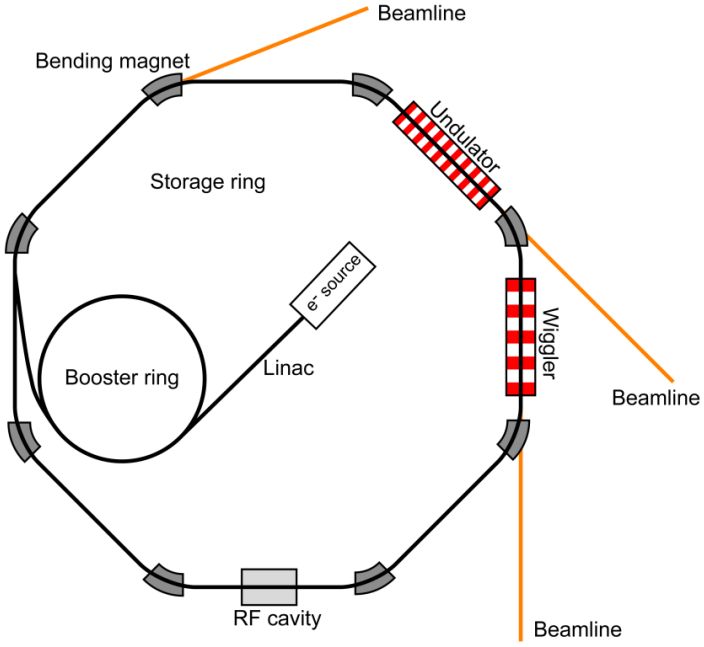


**Figure 4.3.1.** Sketch of a synchrotron showing some of the main components. Electrons are generated and then accelerated before entering the storage ring where synchrotron radiation is produced as the electron beam is bent by bending magnets or insertion devices.

Since the electrons lose energy as they radiate, the energy must be replenished so that they don't collide with the inner wall of the storage ring. This is done by RF cavities that use a high frequency oscillating electric field. The electron beam is not continuous, but consists of electrons grouped together in bunches. Depending on how much energy an electron has lost, it will enter the RF cavity at slightly different points in time and thus experience different electric fields, which helps to keep the electron bunches together travelling at the same speed. In the transverse directions, the beam is kept together by quadrupole and sextupole magnets; the quadrupoles focus the beam and the sextupoles correct for chromatic aberrations caused by the quadrupoles.[174]

The synchrotron radiation is, as previously mentioned, produced by the bending magnets, but can also be produced by so-called insertion devices that

are placed along the straight sections of the storage ring. Such devices use a periodic magnetic structure that forces the electron beam to move in a transverse oscillatory motion to create synchrotron radiation. If the magnetic field is strong, the electron oscillations get large; such an insertion device is known as a *wiggler* and produces much higher photon flux than bending magnets since the beam is bent several times instead of just once. The spectrum of the radiation from a wiggler is broad, similar to that from a bending magnet. If instead the magnetic field is weaker and the electrons oscillate within the divergence angle of the emitted radiation θ, the insertion device is known as an *undulator*. The difference between a wiggler and an undulator is that the emitted synchrotron radiation from each of the bends the beam makes in an undulator overlap and only certain wavelengths interfere constructively, resulting in a spectrum with most of the photon flux narrowly concentrated around those wavelengths. By changing the magnetic field in the undulator by moving the gap between the magnets, the wavelengths that will interfere constructively can be tuned.[174, 177]

The synchrotron radiation emitted from a bending magnet or insertion device travels away from the storage ring and along a beamline where it can be focused, and monochromated before finally reaching the experimental endstation.

## 4.4 Near-edge X-ray absorption fine structure spectroscopy

X-ray absorption in matter is usually a smooth function of photon energy, but at certain energies, sharp, step-like increases in the absorption are found, as can be seen in Figure 4.4.1. These features, called absorption edges, occur at photon energies that match the energy required to ionize a core-level. Looking closer at an absorption edge, one will find that it is in fact not just a step; there is structure to be seen. The region close to the edge can have strong fluctuations in absorption, known as near-edge X-ray absorption fine structure (NEXAFS).

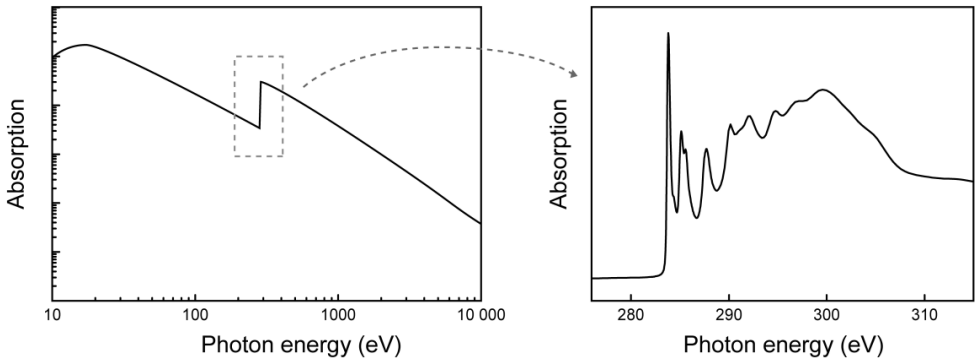


**Figure 4.4.1:** X-ray absorption spectrum showing the carbon K-edge, the right-hand side displaying the NEXAFS region. Left figure adapted from reference 115.

Since variable photon energy is required, NEXAFS measurements are normally performed at synchrotron facilities. As the photon energy is scanned across an absorption edge, core-level electrons get excited into unoccupied states. The spectrum thus gives information about the density of unoccupied states. NEXAFS spectroscopy is not only element sensitive, but also bond sensitive. For example, diamond, graphite and $C_{60}$ have very distinct NEXAFS spectra even though they only contain carbon atoms. Organic molecules have particularly rich and detailed features at the carbon edge,[178] making it possible to use NEXAFS spectra as a way to identify a molecule by its molecular fingerprint. In addition, information about molecular orientation can be obtained from angular resolved NEXAFS since the orientation of a molecular orbital with respect to the electric field of the incident X-rays affect the absorption probability.[179-181]

A NEXAFS spectrum can be recorded in a number of different ways; directly by counting the number of transmitted X-rays and comparing it to the incident

intensity, or indirectly via the relaxation processes that follow the absorption. If any transmitted signal is to be measured, however, the sample must be thin enough to provide a detectable transmission signal, and either mounted on a transparent substrate or freestanding. The relaxation processes work as follows. After a photon has been absorbed and an electron has been promoted from a core level into an unoccupied state, an electron will soon relax and fill the hole in the core level. As this happens, energy is released, either by the emission of a fluorescent photon or by the ejection of an Auger electron. By detecting the emitted photons (known as *fluorescent yield*) or the electrons (known as *electron yield*), a quantitative measure of the absorption is obtained. The different detection modes are illustrated in Figure 4.4.2. The fluorescent yield gives information from deeper within the sample than electron yield, since the escape depth of photons is much higher than for electrons. However, for molecules made of light elements (such as carbon, nitrogen or oxygen), the fluorescent yield is much lower than the electron yield.[182]

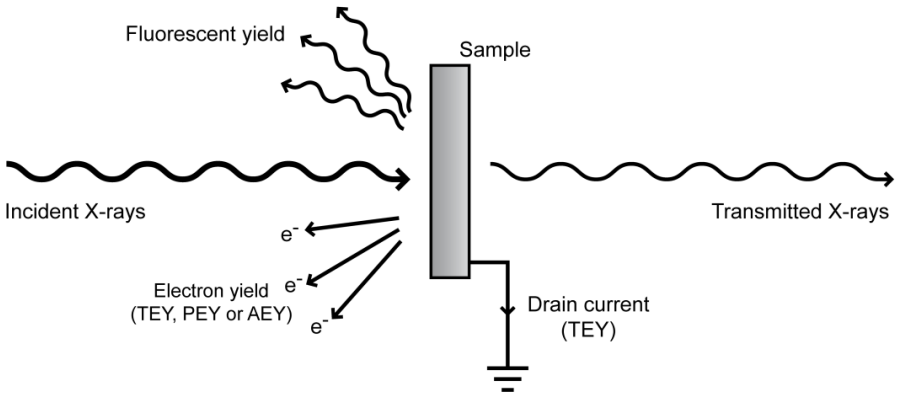


**Figure 4.4.2.** Different detection modes in NEXAFS spectroscopy.

The electron yield can in turn be measured in various ways, giving different surface sensitivity. In total electron yield (TEY), all electrons that manage to escape the sample are counted, often by measuring the sample drain current, but can also be measured using a channeltron. In partial electron yield (PEY), a channeltron is used together with a retarding voltage that prevents low kinetic energy electrons from entering the channeltron. Since electrons originating from deeper within the sample are very likely to have lost energy to inelastic scattering on their way out, the PEY has a higher surface sensitivity than the TEY. If instead an electron energy analyser is used to detect the electrons, the detection window can be chosen to match the kinetic energy of electrons emitted by an Auger transition; i.e. electrons that have lost no energy to

inelastic scattering can selectively be measured. This mode is called Auger electron yield (AEY) and is the most surface sensitive of the different electron yield modes.

Since NEXAFS spectra of organic materials have rich features and can be used as molecular fingerprints, it is possible to deduce the composition of multicomponent blends from the NEXAFS spectra. If the spectra of the pure components are available, the spectrum of the blend can then be fitted to a linear combination of the pure components' spectra. The coefficients in the linear combination then give the volume ratio of the components.[183] This requires that the pure components do not react and form new components when blended. By using detection modes with different surface sensitivities, the composition can be probed at different depths.

## 4.5 Scanning transmission X-ray microscopy

Scanning transmission X-ray microscopy (STXM) is a technique that combines NEXAFS spectroscopy with microscopy, providing composition maps with chemical contrast. In materials that are mixtures of components whose NEXAFS spectra differ, STXM can be used not only to distinguish between the components, but also quantitatively determine the composition. A typical STXM setup is shown in Figure 4.5.1.

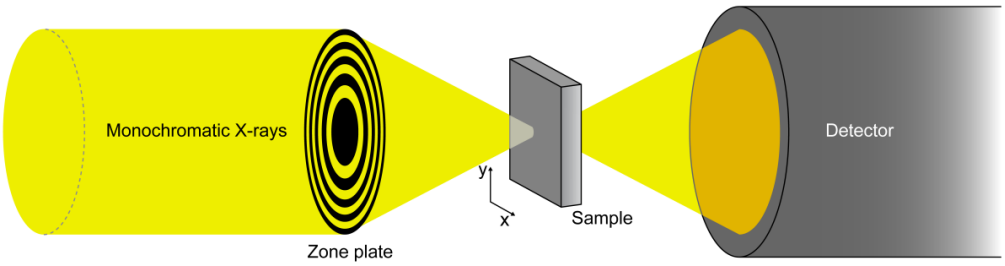


**Figure 4.5.1.** Schematic illustration of a STXM setup. Monochromatic X-rays are focused onto the sample by a zone plate. The sample is raster scanned relative to the beam while the transmitted X-rays are detected. Unwanted diffraction orders from the zone plate are blocked by an order sorting aperture (not shown in the figure).

First of all, the NEXAFS spectra of the pure components are examined to find the photon energies where the difference in absorption is the highest. These photon energies are then selected for image scans. The X-rays are focused onto the sample and the transmitted intensity is recorded as a function of x, y position as the sample is raster scanned, forming a transmission image for a certain photon energy. The focusing is done by a Fresnel zone plate that focuses the light by diffraction, and an order sorting aperture is placed after the zone plate, only letting first order light from the zone plate through. The smallest possible spot size is obtained by using spatially coherent light, and for a given X-ray wavelength, the spot size is limited by the outer zone width of the zone plate.[177] For soft X-rays, using high quality zone plates, spatial resolutions of a few tens of nanometers can be achieved.[177, 184] The fine movement of the sample relative to the beam is typically done in the x- and y-directions by piezoelectric stages, course x, y and z movement by stepper motors.

The STXM composition maps are obtained from the transmission images in a similar manner to how the composition of a blend is deduced by NEXAFS spectroscopy. In the image scans, pixel by pixel, the absorption at each photon energy is fitted to a linear combination of the pure components' absorption. This way, a chemical composition map can be obtained.

Usually, the absorption is measured in transmission mode as shown in Figure 4.5.1. That way, the deduced composition at each pixel will be an average vertically through the sample. However, it is also possible to obtain maps of the surface composition by measuring the absorption from the electron yield. Watts et al. used a channeltron in addition to the more regular X-ray detector to simultaneously measure the bulk and surface composition of a polymer blend.[185]

## 4.6 X-ray photoelectron spectroscopy

X-ray photoelectron spectroscopy (XPS) is a surface sensitive technique that probes the occupied electronic states of a sample. Electrons ejected from the X-ray illuminated sample are collected and their kinetic energy is measured, thus giving information about the core-level or valence band from which they originated. XPS is based on the photoelectric effect[186] and the relation between the electron binding energy $E_B$ and the measured kinetic energy $E_K$ is given by[187]

$$h\nu = E_B + \phi + E_K \tag{4.3}$$

where $h$ is Planck's constant, $\nu$ the photon frequency and $\phi$ the work function of the detector in electrical contact with the sample.

A schematic diagram of a typical XPS experiment is shown in Figure 4.6.1. In contrast to NEXAFS spectroscopy where the photon energy is scanned, XPS uses a fixed excitation energy and measures the kinetic energies of the emitted photoelectrons. This is done by an electron energy analyser, often a concentric hemispherical analyser that uses two concentric hemispheres with a voltage difference between them. For a given voltage and analyser geometry, the electrons will move in different trajectories depending on the kinetic energy, thus enabling the kinetic energy to be measured. Smaller kinetic energy ranges can simultaneously be measured by a position sensitive detector as the electrons exit the hemispheres, while larger ranges are measured by sweeping the voltage difference between the hemispheres. In practice, however, the electrons are often pre-retarded before entering the analyser to a predetermined kinetic energy known as the pass energy, so it is instead the retarding voltage that is swept. The reason for this is to get the same relative energy resolution for all kinetic energies.[174, 187]

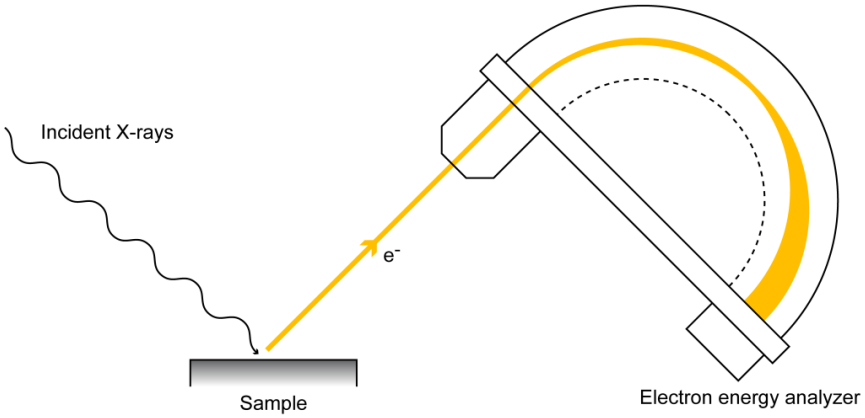


**Figure 4.6.1.** Typical XPS setup. Monochromatic X-rays cause the emission of photoelectrons whose kinetic energy is measured by an electron energy analyser.

Once the kinetic energies are determined using equation 4.3, the binding energies of the different core-level and valence band electrons can be obtained. Since each element has its core levels at unique binding energies XPS allows for the identification of the elemental constituents at a sample's surface as well as their relative concentration. In addition, the binding energy of a core level is affected by the local chemical environment, giving rise to core-level chemical shifts. These shifts can be rather large, for example, the difference between the C1s binding energy in graphite and in carbon dioxide is more than 7 eV.[188]

Not all electrons leaving a sample illuminated by X-rays are directly ejected photoelectrons. After a core level electron has been removed from an atom, an outer shell electron can refill the core level, whereby energy can be released by the emission of an Auger electron. Since the kinetic energy of an Auger electron is determined just by the energy level differences in the atom from which it originated, an Auger peak is easily identified by changing the excitation energy and observing whether the kinetic energy of the peak changes or not.

Another contribution to an XPS spectrum comes from all the electrons that on their way out of the sample lose energy to inelastic scattering. A photoelectron originating from an atom deeper within the sample than the inelastic mean free path is likely to interact inelastically with its surroundings and, apart from losing kinetic energy itself, also produce a cascade of secondary electrons. These electrons will contribute to a background signal; and since electrons with kinetic energy of a few eV have comparably long inelastic mean free paths, the low kinetic energy range of an XPS spectrum is dominated by secondary electrons.

## 4.7 Kelvin probe

First developed in 1898 by Lord Kelvin,[189] the Kelvin probe measures the work function of metals or semiconductors. Unlike many other techniques used to measure work functions, the Kelvin probe is completely nondestructive and does not require the use of high temperature, strong electric fields or beams of photons or electrons.[190]

When two conductive materials become electrically connected, electrons will flow from the low work function material to the high work function material in order to align the Fermi levels. As a result, the low work function material becomes positively charged and the other negatively charged. The potential difference between them, called the contact potential difference $V_{CPD}$, is related to the work function difference between the two materials by[191, 192]

$$V_{CPD} = \frac{\phi_2 - \phi_1}{e} \tag{4.5}$$

where $\phi_1$ and $\phi_2$ are the work functions of the two materials and $e$ the electron charge.

In order to measure the contact potential difference, the two materials are placed to form the plates of a parallel plate capacitor. When electrically connected, the plates will be charged. Changing the distance between the plates changes the capacitance which in turn causes a current to flow. Hence, by making one of the materials vibrate at a certain frequency, an alternating current is generated. If an external voltage is applied and varied until the current vanishes, the external voltage will be equal in magnitude and opposite in polarity to the contact potential difference.[190, 192] If the work function of one of the materials is known, it is then straightforward to calculate the work function of the other using equation 4.5.

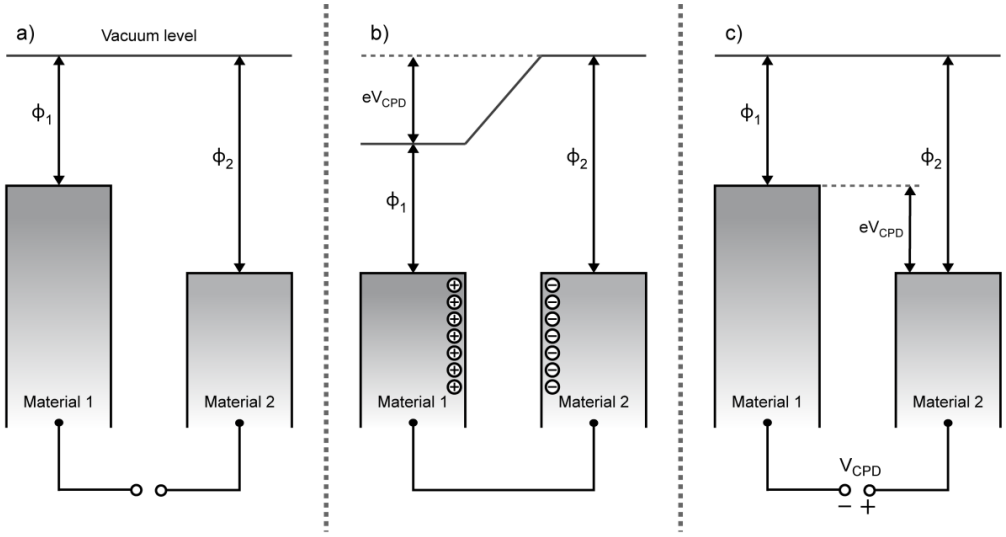


**Figure 4.7.1.** Energy diagram for two materials, illustrating the principle of the Kelvin probe. As two conducting materials with different work functions (a) are brought into electrical contact (b), electrons will flow from the low work function material to the high work function material until the Fermi levels are aligned, thus building up a contact potential difference $V_{CPD}$. By applying an external voltage (c) equal to $V_{CPD}$, the surface charges vanish.

## 4.8 Electron microscopy

The resolution of an optical microscope is ultimately limited by the wavelength of the imaging light.[193] Consequently, visible light cannot be used to resolve objects on the nanometer-scale; instead light with a much shorter wavelength would be needed. X-rays have sufficiently short wavelength and therefore meet this requirement. One type of X-ray microscopy, STXM, is described in section 4.5. Another alternative is to use electrons in microscopes instead of light.

In 1924, de Broglie postulated the wave properties of electrons,[194] which was confirmed experimentally in 1927.[195, 196] At almost the same time, in 1926, Busch had found that an electron beam can be focused by magnetic fields in a manner similar to how light can be focused by optical lenses.[197] Only a few years later, in 1931, the first electron microscope was constructed by Ruska and Knoll.[198]

The wavelength $\lambda$ of an electron with kinetic energy $E_K$ is given by

$$\lambda = \frac{h}{\sqrt{2m_e E_K}} \tag{4.4}$$

where $h$ is Planck's constant and $m_e$ the electron mass.

Even at electron energies as low as a few ten eV, the electron wavelength is three orders of magnitude shorter than the wavelength of visible light. Thus it is clear that electron microscopy, just like X-ray microscopy, is capable of imaging at significantly higher spatial resolution than visible light microscopy. There are of course several fundamental differences between an electron beam and an X-ray beam. Electrons, unlike X-rays, are deflected by electromagnetic fields, which makes focusing an electron beam much more straightforward than focusing X-rays. Furthermore, the penetration depth of an electron beam, although varying with the kinetic energy of the electrons,[199] is much lower than for X-rays. Consequently, surface sensitive measurements are more easily carried out using electron microscopy than for X-ray microscopy, while measurements in transmission mode on samples thicker than a few hundred nanometers are more suitable for X-ray microscopy.[200] Two of the most common types of electron microscopes, the scanning electron microscope (SEM) and the transmission electron microscope (TEM) are described in section 4.8.1 and 4.8.2 respectively.

### 4.8.1 Scanning electron microscopy

In an SEM, electrons from an electron gun are accelerated, usually to energies on the order of 1 - 10 keV, and focused onto the sample by a series of electromagnetic lenses. An image is obtained point by point as the electron beam is raster scanned across the sample. The electrons interact with the sample in various ways, producing different signals that contain information about the sample. These interactions are summarized below in Figure 4.8.1.

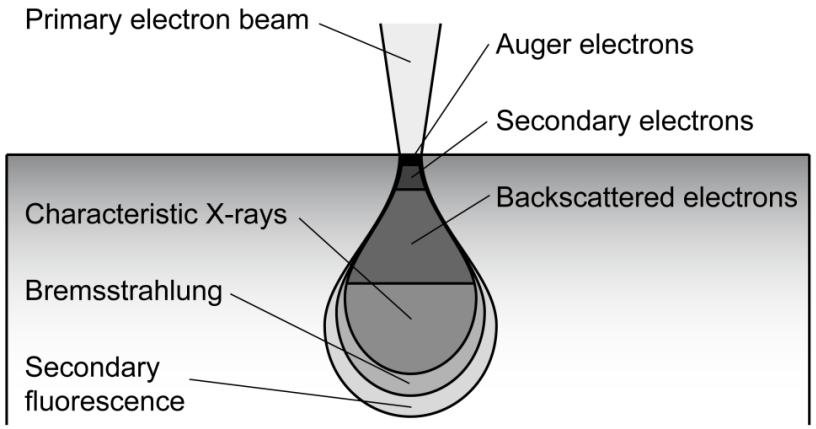


**Figure 4.8.1.** Schematic illustration of the most important electron beam-sample interaction processes in an SEM, showing the outer boundaries of the volumes from which different signals can escape the sample.

As the primary electron beam hits the sample, the electrons will undergo elastic as well as inelastic scattering. The primary electrons will gradually lose energy by the inelastic scattering events and can reach a distance into the sample ranging from a few ten nanometers up to ten micrometers, depending on the energy of the primary electrons and on the atomic number and density of the sample material.[201] The volume that the primary electrons can reach is known as the interaction volume. From within the interaction volume, several different signals, including backscattered electrons, secondary electrons, Auger electrons, characteristic X-rays, Bremsstrahlung and secondary fluorescence originate. The resolution is limited by the size of the electron beam as it hits the sample surface and by the interaction volume of the signal that is being recorded. A typical resolution when detecting secondary electrons is 1 - 10 nm.[201]

Some primary electrons undergo multiple scattering events at large angles and are able to escape through the sample surface. Such electrons are called

backscattered electrons and include, by convention, electrons that have energy above 50 eV.[201] Of course, all electrons leaving the sample with energies above 50 eV need not necessarily be backscattered electrons. Secondary electrons with energies above 50 eV exist, as do backscattered electrons with energies below 50 eV. Nevertheless, the 50 eV threshold for the definition of backscattered electrons is generally considered to be a good approximation.[202] The relative amount of backscattered electrons depends on the atomic number of the sample, hence backscattered electrons can give elemental contrast.

The energy lost by an electron that undergoes inelastic scattering can eject electrons that are bound to atoms in the sample, creating cascades of secondary electrons. Since most of the secondary electrons have a low energy, typically a few eV,[201] only secondary electrons originating from close to the sample surface will have a good chance to escape. Therefore secondary electrons provide a surface sensitive signal. Since the escape depth for secondary electrons is small, on the order of a few nanometers,[201] the number of secondary electrons leaving the surface depends on the angle between the primary beam and the sample surface. If the surface is tilted so that the primary beam hits at a grazing angle, a larger number of secondary electrons will be emitted than if the primary beam hits the sample at normal incidence. This gives rise to topographical contrast when imaging using secondary electrons. Furthermore, secondary electrons from parts of the sample surface that do not have line of sight to the detector will not be effectively detected, giving rise to a shadow effect in the image, as if the sample were illuminated from the position of the detector.

Following an inelastic scattering event in which an electron from the core level of an atom is removed, energy can be released when an outer shell electron fills the vacant core level. Characteristic X-rays and Auger electrons can be emitted this way and both give chemical information about the sample. The signal from the Auger electrons is very surface sensitive, while the characteristic X-rays can originate from much deeper within the sample. In contrast to Auger electrons, the volume from which the characteristic X-rays can originate is not limited by their mean free path in the sample, but rather by the volume that the primary electrons can reach while still having enough remaining kinetic energy to eject a core level electron. However, if more than one type of atom is present in the sample, it is possible for the characteristic X-rays of one element to ionize another element, which then emits X-rays of its own; this is called secondary fluorescence and can be emitted from outside the volume reached by the primary electrons. The volume that can be reached by the primary electrons,

but in which they have lost too much energy to be able to produce characteristic X-rays, can still produce Bremsstrahlung.

### 4.8.2 Transmission electron microscopy

TEMs operate at higher electron energies than SEMs, typically at a few hundred keV. The operational principle of a TEM is analogous to that of a conventional optical microscope. The electron beam is focused onto a very thin sample, preferably no thicker than a few hundred nanometers, that is placed between the electron source and a detector. When passing through the sample, the beam has been made as parallel as possible and broad enough to cover the area of interest. The transmitted electron beam then passes another set of electromagnetic lenses and a magnified image is projected onto the detector. It is also possible to run a TEM in a scanning probe mode where the electron beam is focused into a very small spot and raster scanned across the sample while recording the transmitted electron intensity, building the image point by point. The spatial resolution that can be obtained in TEM is very high, with resolutions below 0.5 Å having been reported.[203]

Image contrast in TEM is due to the interactions between the electron beam and the sample. In crystalline samples, diffracted electrons can be specifically selected or excluded by the use of apertures to give images with diffraction contrast. Amorphous materials can be imaged as well since thickness and density differences also give contrast; areas of the sample that are thick or contain dense materials will scatter electrons more and will appear dark in the TEM image. In polymer:fullerene solar cells, it is the density difference between the fullerenes and the conjugated polymers that allows the two materials to be easily discernable, and consequently TEM is a widespread tool to characterize such films.[204] Problems do arise, however, when trying to use TEM to image the active layer of polymer:polymer solar cells since there may not be any appreciable density difference between two conjugated polymers that will give contrast in the TEM image. There are however, means by which also chemical contrast can be obtained in TEM.

Since the kinetic energy range of the primary electron beam in the TEM can be narrow, it is possible measure the energy lost in the inelastic scattering events by detecting and measuring the kinetic energy of electrons that have been involved in such events. This technique is known as electron energy loss spectroscopy (EELS). Since the inelastic interactions between the primary electrons and the sample atoms include inner shell ionizations, an EELS spectrum contains chemical information. The presence of an element can thus be detected by a corresponding ionization edge in the EELS spectrum. Apart from just elemental composition, it is also possible to look closer at the

ionization edge and study the fine structure to gain information about bonding, and thus obtaining a molecular fingerprint.[205-207] In that sense, EELS shares similarities with NEXAFS spectroscopy as both techniques measure the unoccupied electronic states by core excitations. Just as NEXAFS spectroscopy can be used for imaging with chemical contrast with STXM, so can also EELS be used in combination with TEM. There are however some differences between STXM and TEM-EELS. While the spatial resolution for TEM is two orders of magnitude higher than for STXM, the energy resolution for STXM is higher.[208] Furthermore, the radiation damage is about 100 – 1000 times higher for TEM-EELS than for STXM since a large part of the electron energy losses are damaging the sample.[207, 208] Also only a small fraction of those electron energy losses are detectable, whereas every photon absorption event in STXM is detectable.

# Chapter 5
# Introduction to the papers

## Paper I

In this paper, the effect of the choice of solvent and the use of the additive chloronaphthalene in the coating process on the morphology of thin films of TQ1:$PC_{70}BM$ blends is studied. The lateral morphology of the active layer of the solar cell was probed by AFM and STXM, the vertical morphology by SIMS and ellipsometry, and the surface composition by NEXAFS spectroscopy. The results show lateral phase-separated domains in films spin-coated from single solvents, with $PC_{70}BM$ rich islands surrounded by a TQ1 rich phase. The lateral domain size increases with increasing solvent vapour pressure and decreasing $PC_{70}BM$ solubility. When small amounts of chloronaphthalene are added to the coating solution no such lateral domains are observed. At the surface of the film a strongly TQ1-enriched layer is found in all TQ1:$PC_{70}BM$ blends, rationalized by surface energy differences between TQ1 and $PC_{70}BM$. The influence of the active layer morphology on the solar cell performance is also studied. The addition of chloronaphthalene strongly improves the photocurrent and power conversion efficiency, correlated to finer lateral domain sizes and higher TQ1-enrichment at the cathode interface. Neither the open-circuit voltage nor the series resistance of the devices are sensitive to the differences in morphology. This indicates that the TQ1 enriched surface layer does not hinder charge transport and collection.

## Paper II

In this paper, the photo-degradation of a TQ1:PCBM blend is studied. Changes to the electronic structure of TQ1 and PCBM caused by illumination of films in ambient air are investigated and the photo-degradation in pristine materials and the blend are compared. The effect of the photo-degradation on the solar cell performance is also studied. NEXAFS spectroscopy shows that the unoccupied molecular orbitals of TQ1 are not significantly affected, while those of PCBM are severely degraded in pristine films. PCBM blended with TQ1 is found to degrade even faster than pristine PCBM. The occupied molecular orbitals of TQ1 exhibit changes upon light exposure, seen in the valence band spectrum, and photo-bleaching of TQ1 is observed. Solar cells in which the active layer has been exposed to light in air before depositing the top electrode show a greatly reduced performance. The photo-bleaching of TQ1 is not large enough

to explain these losses, which are mainly attributed to the PCBM degradation at the surface of the active layer.

## Paper III

In this manuscript, the use of solution processed $NiO_x$ thin films as the hole transport layer in TQ1:$PC_{70}BM$ solar cells is studied. The $NiO_x$ films are prepared without the need for high temperature annealing, by partially or even completely replacing the annealing step with exposure to UV-ozone. The $NiO_x$ films produced this way outperform PEDOT:PSS. The power conversion efficiency improves from 5.3% to 6.1% when replacing PEDOT:PSS with $NiO_x$, mainly as a result of an increased fill factor. The chemical composition of the $NiO_x$ is investigated by XPS and is compared to $NiO_x$ thin films produced by conventional high temperature annealing. While high temperature annealing produces NiO, the UV-ozone treatment leads to the formation of a mixture of oxides and hydroxides. Contact potential difference measurements reveal an increased work function for all UV-ozone treated $NiO_x$ films, consistent with the presence of NiOOH at the surface. The use of the high work function UV-ozone treated $NiO_x$ films improves the energy level matching between the donor and the hole transport layer, resulting in an improved hole injection and enhanced solar cell efficiency.

## Paper IV

In this manuscript, the possibilities and some of the challenges in using NEXAFS spectroscopy and STXM for characterization of blend films for organic photovoltaics are treated. Quantitative determination of the local chemical composition requires careful use of fitting techniques, as well as suitable sample preparation and handling. For microscopy studies in transmission mode, the films are typically floated off from PEDOT:PSS-coated substrates onto water and then collected on Cu grids. Here, drop-like clusters, ~1 μm in diameter are observed at the bottom of the films. STXM confirms that the clusters consist of nearly pure $PC_{70}BM$. In films spincoated directly onto PEDOT:PSS-covered $Si_3N_4$ membranes, such clusters are not observed. The $PC_{70}BM$ clusters are therefore formed during transfer of the films onto Cu grids, showing that contact with water can modify the film and influence the composition in polymer:fullerene blend films. It is also demonstrated how the formation of these drop-like clusters of $PC_{70}BM$ leads to an underestimation of $PC_{70}BM$/polymer concentration ratios. Finally, it is shown that selective

degradation of one of the blend components can impair accurate determination of the local blend composition.

## Paper V

In this manuscript the rapid initial photo-degradation of the electrical performance, the so-called burn-in, is studied in encapsulated PCDTBT:$PC_{70}BM$ solar cells. Solar cells using PEDOT:PSS as the hole transport material exhibit a rapid drop in $V_{OC}$ of around 100 mV during the first sun-hours of illumination. This $V_{OC}$ drop occurs both when the solar cells are exposed to light with and without a UV-component and also for light intensities between 1 sun and 100 suns. As the $V_{OC}$ drops, the shape of the JV-curve is maintained as it is shifted towards lower voltages. By replacing the PEDOTS:PSS with $MoO_3$, the initial loss in $V_{OC}$ is significantly reduced, thus showing that the $V_{OC}$ loss is directly related to the PEDOT:PSS. With the help of numerical drift-diffusion simulations, the origin of this effect is further analysed. Several mechanisms that previously have been suggested as the origin of the burn-in are investigated, and their validity for this specific case is discussed.

# Chapter 6
# Conclusions

The work presented in this thesis shows how the active layer morphology, the choice of hole transport layer material, the photo-degradation of the active layer components and the electrical performance of polymer solar cells are related to one another.

Being able to control the nanostructure is of great importance for producing efficient polymer solar cells. The results in this thesis demonstrate how, for TQ1:$PC_{70}BM$ blends, the solution formulation can influence the active layer morphology and how that, in turn, affects the solar cell performance. The laterally phase-separated structures are chemically identified using STXM, showing that $PC_{70}BM$-rich islands are surrounded by a TQ1-rich phase. The TQ1-enrichment found at the surface of the active layer does not appear to hinder charge transport and collection.

In order to correctly determine the local composition in polymer:fullerene blend films by soft X-ray spectroscopy techniques, care has to be taken so that the fitting technique, sample preparation and handling do not influence the results. Direct contact between the film and water, as is common when transferring films to Cu grids for TEM or STXM analysis, can lead to the formation of micrometer-sized fullerene clusters. Exposure to light in air causes selective degradation of PCBM which can lead to an underestimation of the PCBM content in the film.

The photo-degradation of a TQ1:PCBM blend in air and its effect on the solar cell performance is also studied. It is shown that PCBM degrades faster in the blend film than in a pristine film rationalized by the higher light absorption and subsequent electron transfer by TQ1, and the reduced solar cell performance is mainly attributed to the PCBM degradation.

Solution processed $NiO_x$ films, prepared by UV-ozone treatment without need for high temperature annealing, can be used as the hole transport layer in polymer solar cells and outperform the commonly used PEDOT:PSS. The efficiency improves mainly as a result of an increased fill factor, which is due to the higher work function of UV-ozone treated $NiO_x$ films, which improves the energy level matching between the donor and the hole transport layer and results in an improved hole injection.

The rapid initial photo-degradation of the electrical performance of encapsulated PCDTBT:$PC_{70}BM$ solar cells was found to be directly related to the PEDOT:PSS hole transporting layer. By replacing the PEDOT:PSS with $MoO_3$, the initial degradation was greatly reduced. Using drift-diffusion simulations, the origin of this effect was further analysed and previously suggested mechanisms were investigated.

## References


1 U.S. Energy Information Administration, *International Energy Outlook 2013*, **2013.**

2 G. Kopp, G. Lawrence and G. Rottman, *Sol. Phys.*, **2005**, 230, 129-139.

3 International Energy Agency, *Solar energy perspectives*, **2011.**

4 A. E. Becquerel, *Comptes Rendus*, **1839**, 9, 561-567.

5 W. Smith, *Science*, **1873**, 7, 303.

6 C. E. Fritts, *American Journal of Science*, **1883**, 26, 465-472.

7 D. M. Chapin, C. S. Fuller and G. L. Pearson, *J. Appl. Phys.*, **1954**, 25, 676-677.

8 M. A. Green, K. Emery, Y. Hishikawa, W. Warta and E. D. Dunlop, *Prog. Photovolt: Res. Appl.*, **2015**, 23, 1-9.

9 International Energy Agency, *A Snapshot of Global PV 1992-2013*, **2014.**

10 W. Shockley and H. J. Queisser, *J. Appl. Phys.*, **1961**, 32, 510-519.

11 R. Søndergaard, M. Hösel, D. Angmo, T. T. Larsen-Olsen and F. C. Krebs, *Mater. Today*, **2012**, 15, 36-49.

12 Z. Zhang, X. Li, G. Guan, S. Pan, Z. Zhu, D. Ren and H. Peng, *Angew. Chem. Int. Ed.*, **2014**, 53, 11571-11574.

13 Heliatek reaches efficiency record with 40% transparent organic solar cells. (www.heliatek.com/newscenter/latest_news/heliatek-erzielt-effizienzrekord-mit-40-transparenten-organischen-solarzellen). Heliatek GmbH, Accessed March 10, 2015.

14 Y. Li, *Acc. Chem. Res.*, **2012**, 45, 723-733.

15 C. J. Brabec, M. Heeney, I. McCulloch and J. Nelson, *Chem. Soc. Rev.*, **2011**, 40, 1185-99.

16 M. A. Brady, G. M. Su and M. L. Chabinyc, *Soft Matter*, **2011**, 7, 11065.

17 M. A. Ruderer and P. Müller-Buschbaum, *Soft Matter*, **2011**, 7, 5482.

18 H. Hoppe and N. S. Sariciftci, *J. Mater. Chem.*, **2006**, 16, 45-61.

19 B. Azzopardi, C. J. M. Emmott, A. Urbina, F. C. Krebs, J. Mutale and J. Nelson, *Energy Environ. Sci.*, **2011**, 4, 3741-3753.

20 D. Angmo and F. C. Krebs, *Energy Technol.*, **2015**, 3, 774-783.

21 A. Pochettino and A. Sella, *Acad. Lincei Rend.*, **1906**, 15, 355-369.

22 H. Kallmann and M. Pope, *J. Chem. Phys.*, **1959**, 30, 585-586.

23 H. Hoegl, O. Süs and W. Neugebauer, *German Patent 1068115*, **1957**,

24 H. Hoegl, *J. Phys. Chem.*, **1965**, 69, 755-766.

25 C. K. Chiang, C. R. Fincher, Y. W. Park, A. J. Heeger, H. Shirakawa, E. J. Louis, S. C. Gau and A. G. MacDiarmid, *Phys. Rev. Lett.*, **1977**, 39, 1098-1101.

26 H. Shirakawa, E. J. Louis, A. G. MacDiarmid, C. K. Chiang and A. J. Heeger, *J. Chem. Soc. Chem. Commun.*, **1977**, 578-580.

27 M. C. Petty, M. R. Bryce and D. Bloor, *Introduction to molecular electronics*, Edward Arnold, London, **1995**.

28 S. S. Sun and L. R. Dalton, *Introduction to Organic Electronic and Optoelectronic Materials and Devices*, CRC Press, Boca Raton, **2008**.

29 W. R. Salaneck, R. H. Friend and J. L. Brédas, *Phys. Rep.*, **1999**, 319, 231-251.

30 M. Schwoerer and H. C. Wolf, *Organic Molecular Solids*, Wiley-VCH Verlag, Weinheim, **2007**.

31 H. Hoppe and N. S. Sariciftci, *J. Mater. Res.*, **2004**, 19, 1924-1945.

32 W. Brütting, *Physics of organic semiconductors*, Wiley-VCH Verlag, Weinheim, **2005**.

33 J.-L. Bredas, J. Cornil and A. J. Heeger, *Adv. Mater.*, **1996**, 8, 447-452.

34 N. S. Sariciftci, L. Smilowitz, A. J. Heeger and F. Wudl, *Synth. Met.*, **1993**, 59, 333-352.

35 B. A. Collins, J. R. Tumbleston and H. Ade, *J. Phys. Chem. Lett.*, **2011**, 2, 3135-3145.

36 O. V. Mikhnenko, H. Azimi, M. Scharber, M. Morana, P. W. M. Blom and M. A. Loi, *Energy Environ. Sci.*, **2012** 5, 6960-6965.

37 T. Stübinger and W. Brütting, *J. Appl. Phys.*, **2001**, 90, 3632.

38 K. Vandewal, A. Gadisa, W. D. Oosterbaan, S. Bertho, F. Banishoeib, I. Van Severen, L. Lutsen, T. J. Cleij, D. Vanderzande and J. V. Manca, *Adv. Funct. Mater.*, **2008**, 18, 2064-2070.

39 K. Vandewal, K. Tvingstedt, A. Gadisa, O. Inganas and J. V. Manca, *Nat. Mater.*, **2009**, 8, 904-909.

40 M. Gerhard, A. P. Arndt, I. A. Howard, A. Rahimi-Iman, U. Lemmer and M. Koch, *J. Phys. Chem. C*, **2015**, 119, 28309-28318.

41 R. Po, C. Carbonera, A. Bernardi and N. Camaioni, *Energy Environ. Sci.*, **2011**, 4, 285-310.

42 R. A. Janssen and J. Nelson, *Adv. Mater.*, **2013**, 25, 1847-1858.

43 W. Shockley, *Electrons and holes in semiconductors*, D. Van Nostrand Company, New York, **1950**.

44 J. Nelson, *The Physics of Solar Cells*, Imperial College Press, London, **2004**.

45 M. C. Scharber, D. Mühlbacher, M. Koppe, P. Denk, C. Waldauf, A. J. Heeger and C. J. Brabec, *Adv. Mater.*, **2006**, 18, 789-794.

46 B. Qi and J. Wang, *Phys. Chem. Chem. Phys.*, **2013**, 15, 8972-8982.

47 American Society for Testing and Materials, . (http://rredc.nrel.gov/solar/spectra/am1.5/). Accessed July 18, 2015.

48 E. A. Katz, A. Mescheloff, I. Visoly-Fisher and Y. Galagan, *Sol. Energy Mater. Sol. Cells*, **2016**, 144, 273-280.

49 L. Schmidt-Mende and J. Weickert, *Organic and Hybrid Solar Cells*, Walter de Gruyter, Berlin, **2016**.

50 E. Zimmermann, P. Ehrenreich, T. Pfadler, J. A. Dorman, J. Weickert and L. Schmidt-Mende, *Nat. Photonics*, **2014**, 8, 669-672.

51 J. Peet, A. J. Heeger and G. C. Bazan, *Acc. Chem. Res.*, **2009**, 42, 1700-1708.

52 B. Kippelen and J.-L. Brédas, *Energy Environ. Sci.*, **2009**, 2, 251-261.

53 A. Salleo, R. J. Kline, D. M. DeLongchamp and M. L. Chabinyc, *Adv. Mater.*, **2010**, 22, 3812-3838.

54 F. Liu, Y. Gu, J. W. Jung, W. H. Jo and T. P. Russell, *J. Polym. Sci. Part B: Polym. Phys.*, **2012**, 50, 1018-1044.

55 C. W. Tang, *Appl. Phys. Lett.*, **1986**, 48, 183-185.

56 G. Yu, J. Gao, J. C. Hummelen, F. Wudl and A. J. Heeger, *Science*, **1995**, 270, 1789-1791.

57 J. J. M. Halls, C. A. Walsh, N. C. Greenham, E. A. Marseglia, R. H. Friend, S. C. Moratti and A. B. Holmes, *Nature*, **1995**, 376, 498.

58 S. E. Shaheen, C. J. Brabec, N. S. Sariciftci, F. Padinger, T. Fromherz and J. C. Hummelen, *Appl. Phys. Lett.*, **2001**, 78, 841-843.

59 F. Zhang, K. G. Jespersen, C. Björström, M. Svensson, M. R. Andersson, V. Sundström, K. Magnusson, E. Moons, A. Yartsev and O. Inganäs, *Adv. Funct. Mater.*, **2006**, 16, 667-674.

60 Y. Yao, J. Hou, Z. Xu, G. Li and Y. Yang, *Adv. Funct. Mater.*, **2008**, 18, 1783-1789.

61 H.-C. Liao, C.-C. Ho, C.-Y. Chang, M.-H. Jao, S. B. Darling and W.-F. Su, *Mater. Today*, **2013**, 16, 326-336.

62 M. T. Rispens, A. Meetsma, R. Rittberger, C. J. Brabec, N. S. Sariciftci and J. C. Hummelen, *Chem. Commun.*, **2003**, 2116-2118.

63 A. C. Arias, *J. Macromol. Sci., Part C: Polym. Rev.*, **2006**, 46, 103-125.

64 C. M. Björström, S. Nilsson, A. Bernasik, J. Rysz, A. Budkowski, F. Zhang, O. Inganäs, M. R. Andersson, K. O. Magnusson and E. Moons, *Proc. SPIE*, **2006**, 6192, 61921X.

65 H. Hoppe, M. Niggemann, C. Winder, J. Kraut, R. Hiesgen, A. Hinsch, D. Meissner and N. S. Sariciftci, *Adv. Funct. Mater.*, **2004**, 14, 1005-1011.

66 C. M. Björström, A. Bernasik, J. Rysz, A. Budkowski, S. Nilsson, M. Svensson, M. R. Andersson, K. O. Magnusson and E. Moons, *J. Phys.: Condens. Matter*, **2005**, 17, L529-L534.

67 A. S. Anselmo, L. Lindgren, J. Rysz, A. Bernasik, A. Budkowski, M. R. Andersson, K. Svensson, J. van Stam and E. Moons, *Chem. Mater.*, **2011**, 23, 2295-2302.

68 A. S. Anselmo, A. Dzwilewski, K. Svensson and E. Moons, *J. Polym. Sci. Part B: Polym. Phys.*, **2013**, 51, 176-182.

69 Z. Xu, L.-M. Chen, G. Yang, C.-H. Huang, J. Hou, Y. Wu, G. Li, C.-S. Hsu and Y. Yang, *Adv. Funct. Mater.*, **2009**, 19, 1227-1234.

70 R. A. L. Jones, E. J. Kramer, M. H. Rafailovich, J. Sokolov and S. A. Schwarz, *Phys. Rev. Lett.*, **1989**, 62, 280-283.

71 S. Y. Heriot and R. A. L. Jones, *Nat. Mater.*, **2005**, 4, 782-786.

72 S. Nilsson, A. Bernasik, A. Budkowski and E. Moons, *Macromolecules*, **2007**, 40, 8291-8301.

73 J. Raczkowska, A. Bernasik, A. Budkowski, K. Sajewicz, B. Penc, J. Lekki, M. Lekka, J. Rysz, K. Kowalski and P. Czuba, *Macromolecules*, **2004**, 37, 7308-7315.

74 M. Jørgensen, K. Norrman, S. A. Gevorgyan, T. Tromholt, B. Andreasen and F. C. Krebs, *Adv. Mater.*, **2012**, 24, 580-612.

75 M. Jørgensen, K. Norrman and F. C. Krebs, *Sol. Energy Mater. Sol. Cells*, **2008**, 92, 686-714.

76 M. P. de Jong, L. J. van Ijzendoorn and M. J. A. de Voigt, *Appl. Phys. Lett.*, **2000**, 77, 2255-2257.

77 K. Kawano, R. Pacios, D. Poplavskyy, J. Nelson, D. D. C. Bradley and J. R. Durrant, *Sol. Energy Mater. Sol. Cells*, **2006**, 90, 3520-3530.

78 K. Norrman and F. C. Krebs, *Sol. Energy Mater. Sol. Cells*, **2006**, 90, 213-227.

79 M. O. Reese, A. M. Nardes, B. L. Rupert, R. E. Larsen, D. C. Olson, M. T. Lloyd, S. E. Shaheen, D. S. Ginley, G. Rumbles and N. Kopidakis, *Adv. Funct. Mater.*, **2010**, 20, 3476-3483.

80 A. Rivaton, S. Chambon, M. Manceau, J.-L. Gardette, N. Lemaître and S. Guillerez, *Polym. Degrad. Stab.*, **2010**, 95, 278-284.

81 N. Grossiord, J. M. Kroon, R. Andriessen and P. W. M. Blom, *Org. Electron.*, **2012**, 13, 432-456.

82 N. K. Elumalai and A. Uddin, *Energy Environ. Sci.*, **2016**, 9, 391-410.

83 M. Glatthaar, M. Riede, N. Keegan, K. Sylvester-Hvid, B. Zimmermann, M. Niggemann, A. Hinsch and A. Gombert, *Sol. Energy Mater. Sol. Cells*, **2007**, 91, 390-393.

84 F. C. Krebs and K. Norrman, *Prog. Photovolt: Res. Appl.*, **2007**, 15, 697-712.

85 C. J. Brabec, S. E. Shaheen, C. Winder, N. S. Sariciftci and P. Denk, *Appl. Phys. Lett.*, **2002**, 80, 1288-1290.

86 K. Kawano and C. Adachi, *Appl. Phys. Lett.*, **2010**, 96, 053307.

87 S. K. M. Jönsson, E. Carlegrim, F. Zhang, W. R. Salaneck and M. Fahlman, *Jpn. J. Appl. Phys.*, **2005**, 44, 3695-3701.

88 P. Henriksson, C. Lindqvist, B. Abdisa, E. Wang, Z. George, R. Kroon, C. Müller, T. Yohannes, O. Inganäs and M. R. Andersson, *Sol. Energy Mater. Sol. Cells*, **2014**, 130, 138-143.

89 A. Seemann, T. Sauermann, C. Lungenschmied, O. Armbruster, S. Bauer, H. J. Egelhaaf and J. Hauch, *Sol. Energy*, **2011**, 85, 1238-1249.

90 M. Manceau, E. Bundgaard, J. E. Carlé, O. Hagemann, M. Helgesen, R. Søndergaard, M. Jørgensen and F. C. Krebs, *J. Mater. Chem.*, **2011**, 21, 4132-4141.

91 E. T. Hoke, I. T. Sachs-Quintana, M. T. Lloyd, I. Kauvar, W. R. Mateker, A. M. Nardes, C. H. Peters, N. Kopidakis and M. D. McGehee, *Adv. Energy Mater.*, **2012**, 2, 1351-1357.

92 A. Tournebize, P.-O. Bussière, A. Rivaton, J.-L. Gardette, H. Medlej, R. C. Hiorns, C. Dagron-Lartigau, F. C. Krebs and K. Norrman, *Chem. Mater.*, **2013**, 25, 4522-4528.

93 B. Watts, W. J. Belcher, L. Thomsen, H. Ade and P. C. Dastoor, *Macromolecules*, **2009**, 42, 8392-8397.

94 C. Lindqvist, A. Sanz-Velasco, E. Wang, O. Bäcke, S. Gustafsson, E. Olsson, M. R. Andersson and C. Müller, *J. Mater. Chem. A*, **2013**, 1, 7174-7180.

95 B. Conings, S. Bertho, K. Vandewal, A. Senes, J. D'Haen, J. Manca and R. A. J. Janssen, *Appl. Phys. Lett.*, **2010**, 96, 163301.

96 S. Bertho, I. Haeldermans, A. Swinnen, W. Moons, T. Martens, L. Lutsen, D. Vanderzande, J. Manca, A. Senes and A. Bonfiglio, *Sol. Energy Mater. Sol. Cells*, **2007**, 91, 385-389.

97 S. Chambon, A. Rivaton, J.-L. Gardette and M. Firon, *Sol. Energy Mater. Sol. Cells*, **2007**, 91, 394-398.

98 A. S. Anselmo, A. Dzwilewski, K. Svensson and E. Moons, *Chem. Phys. Lett.*, **2016**, 652, 220-224.

99 Q. Bao, X. Liu, S. Braun and M. Fahlman, *Adv. Energy Mater.*, **2014**, 4, 1301272.

100 F. C. Krebs, *Stability and Degradation of Organic and Polymer Solar Cells*, John Wiley & Sons, Chichester, **2012**.

101 F. C. Krebs, *Sol. Energy Mater. Sol. Cells*, **2006**, 90, 3633-3643.

102 Y. Leterrier, *Prog. Mater. Sci.*, **2003**, 48, 1-55.

103 E. H. H. Jamieson and A. H. Windle, *J. Mater. Sci.*, **1983**, 18, 64-80.

104 S. Schuller, P. Schilinsky, J. Hauch and C. J. Brabec, *Appl. Phys. A*, **2004**, 79, 37-40.

105 E. Voroshazi, B. Verreet, A. Buri, R. Müller, D. Di Nuzzo and P. Heremans, *Org. Electron.*, **2011**, 12, 736-744.

106 M. V. Madsen, T. Tromholt, K. Norrman and F. C. Krebs, *Adv. Energy Mater.*, **2013**, 3, 424-427.

107 J. M. Gordon, E. A. Katz, D. Feuermann and M. Huleihil, *Appl. Phys. Lett.*, **2004**, 84, 3642-3644.

108 T. Tromholt, M. Manceau, M. Helgesen, J. E. Carlé and F. C. Krebs, *Sol. Energy Mater. Sol. Cells*, **2011**, 95, 1308-1314.

109 I. Visoly-Fisher, A. Mescheloff, M. Gabay, C. Bounioux, L. Zeiri, M. Sansotera, A. E. Goryachev, A. Braun, Y. Galagan and E. A. Katz, *Sol. Energy Mater. Sol. Cells*, **2015**, 134, 99-107.

110 B. J. Worfolk, S. C. Andrews, S. Park, J. Reinspach, N. Liu, M. F. Toney, S. C. B. Mannsfeld and Z. Bao, *Proc. Natl. Acad. Sci. USA*, **2015**, 112, 14138-14143.

111 C. Badre, L. Marquant, A. M. Alsayed and L. A. Hough, *Adv. Funct. Mater.*, **2012**, 22, 2723-2727.

112 N. Koch, A. Kahn, J. Ghijsen, J. J. Pireaux, J. Schwartz, R. L. Johnson and A. Elschner, *Appl. Phys. Lett.*, **2003**, 82, 70-72.

113 C. Tengstedt, A. Crispin, C. Hsu, C. Zhang, I. Parker, W. Salaneck and M. Fahlman, *Org. Electron.*, **2005**, 6, 21-33.

114 K. Norrman, M. V. Madsen, S. A. Gevorgyan and F. C. Krebs, *J. Am. Chem. Soc.*, **2010**, 132, 16883-16892.

115 I. Etxebarria, J. Ajuria and R. Pacios, *Org. Electron.*, **2015**, 19, 34-60.

116 N. Koch, A. Vollmer and A. Elschner, *Appl. Phys. Lett.*, **2007**, 90, 043512.

117 A. Elschner, S. Kirchmeyer, W. Lovenich, U. Merker and K. Reuter, *PEDOT: Principles and Applications of an Intrinsically Conductive Polymer*, CRC Press, Boca Raton, **2010**.

118 W. C. Choy and D. Zhang, *Small*, **2016**, 12, 416-431.

119 L.-M. Chen, Z. Xu, Z. Hong and Y. Yang, *J. Mater. Chem.*, **2010**, 20, 2575-2598.

120 F. Wang, Z. a. Tan and Y. Li, *Energy Environ. Sci.*, **2015**, 8, 1059-1091.

121 J. Meyer, S. Hamwi, M. Kroger, W. Kowalsky, T. Riedl and A. Kahn, *Adv. Mater.*, **2012**, 24, 5408-5427.

122 M. D. Irwin, D. B. Buchholz, A. W. Hains, R. P. H. Chang and T. J. Marks, *Proc. Natl. Acad. Sci. USA*, **2008**, 105, 2783-2787.

123 M. T. Greiner, M. G. Helander, W. M. Tang, Z. B. Wang, J. Qiu and Z. H. Lu, *Nat. Mater.*, **2011**, 11, 76-81.

124 J. Meyer, K. Zilberberg, T. Riedl and A. Kahn, *J. Appl. Phys.*, **2011**, 110, 033710.

125 M. Kröger, S. Hamwi, J. Meyer, T. Riedl, W. Kowalsky and A. Kahn, *Appl. Phys. Lett.*, **2009**, 95, 123301.

126 J. G. Aiken and A. G. Jordan, *J. Phys. Chem. Solids*, **1968**, 29, 2153-2167.

127 M. A. Wittenauer and L. L. v. Zandt, *Philos. Mag. B*, **1982**, 46, 659-667.

128 F. J. Morin, *Phys. Rev.*, **1954**, 93, 1199-1204.

129 D. Adler and J. Feinleib, *Phys. Rev. B*, **1970**, 2, 3112-3134.

130 S. Lany, J. Osorio-Guillén and A. Zunger, *Phys. Rev. B*, **2007**, 75, 241203.

131 K. X. Steirer, P. F. Ndione, N. E. Widjonarko, M. T. Lloyd, J. Meyer, E. L. Ratcliff, A. Kahn, N. R. Armstrong, C. J. Curtis, D. S. Ginley, J. J. Berry and D. C. Olson, *Adv. Energy Mater.*, **2011**, 1, 813-820.

132 K. X. Steirer, J. P. Chesin, N. E. Widjonarko, J. J. Berry, A. Miedaner, D. S. Ginley and D. C. Olson, *Org. Electron.*, **2010**, 11, 1414-1418.

133 J. R. Manders, S.-W. Tsang, M. J. Hartel, T.-H. Lai, S. Chen, C. M. Amb, J. R. Reynolds and F. So, *Adv. Funct. Mater.*, **2013**, 23, 2993-3001.

134 J. J. Berry, N. E. Widjonarko, B. A. Bailey, A. K. Sigdel, D. S. Ginley and D. C. Olson, *IEEE J. Sel. Top. Quantum Electron.*, **2010**, 16, 1649-1655.

135 W. Yu, L. Shen, S. Ruan, F. Meng, J. Wang, E. Zhang and W. Chen, *Sol. Energy Mater. Sol. Cells*, **2012**, 98, 212-215.

136 C. C. Hsu, H. W. Su, C. H. Hou, J. J. Shyue and F. Y. Tsai, *Nanotechnology*, **2015**, 26, 385201.

137 J. W. Shim, C. Fuentes-Hernandez, A. Dindar, Y. Zhou, T. M. Khan and B. Kippelen, *Org. Electron.*, **2013**, 14, 2802-2808.

138 J. Kettle, H. Waters, M. Horie and S. W. Chang, *J. Phys. D: Appl. Phys.*, **2012**, 45, 125102.

139 R. Betancur, M. Maymó, X. Elias, L. T. Vuong and J. Martorell, *Sol. Energy Mater. Sol. Cells*, **2011**, 95, 735-739.

140 E. L. Ratcliff, J. Meyer, K. X. Steirer, A. Garcia, J. J. Berry, D. S. Ginley, D. C. Olson, A. Kahn and N. R. Armstrong, *Chem. Mater.*, **2011**, 23, 4988-5000.

141 A. Garcia, G. C. Welch, E. L. Ratcliff, D. S. Ginley, G. C. Bazan and D. C. Olson, *Adv. Mater.*, **2012**, 24, 5368-5373.

142 F. Wang, G. Sun, C. Li, J. Liu, S. Hu, H. Zheng, Z. Tan and Y. Li, *ACS Appl. Mater. Interfaces*, **2014**, 6, 9458-9465.

143 Z. Zhai, X. Huang, M. Xu, J. Yuan, J. Peng and W. Ma, *Adv. Energy Mater.*, **2013**, 3, 1614-1622.

144 K. X. Steirer, R. E. Richards, A. K. Sigdel, A. Garcia, P. F. Ndione, S. Hammond, D. Baker, E. L. Ratcliff, C. Curtis, T. Furtak, D. S. Ginley, D. C. Olson, N. R. Armstrong and J. J. Berry, *J. Mater. Chem. A*, **2015**, 3, 10949-10958.

145 K. Kiriishi, K. Hashiba, J. Qiu, T. Yanagidate, M. Ohzeki, S. Fujii, H. Kataura and Y. Nishioka, *Mol. Cryst. Liq. Cryst.*, **2015**, 620, 38-44.

146 J. Zhang, J. Wang, Y. Fu, B. Zhang and Z. Xie, *J. Mater. Chem. C*, **2014**, 2, 8295-8302.

147 T. Yamamoto, B.-L. Lee, H. Kokubo, H. Kishida, K. Hirota, T. Wakabayashi and H. Okamoto, *Macromol. Rapid Commun.*, **2003**, 24, 440-443.

148 E. Wang, L. Hou, Z. Wang, S. Hellstrom, F. Zhang, O. Inganäs and M. R. Andersson, *Adv. Mater.*, **2010**, 22, 5240-5244.

149 Y. Kim, H. R. Yeom, J. Y. Kim and C. Yang, *Energy Environ. Sci.*, **2013**, 6, 1909-1916.

150 E. E. Havinga, W. t. Hoeve and H. Wynberg, *Polymer Bulletin*, **1992**, 29, 119-126.

151 J. E. Carlé, M. Jørgensen, M. Manceau, M. Helgesen, O. Hagemann, R. Søndergaard and F. C. Krebs, *Sol. Energy Mater. Sol. Cells*, **2011**, 95, 3222-3226.

152 N. Blouin, A. Michaud and M. Leclerc, *Adv. Mater.*, **2007**, 19, 2295-2300.

153 Y. Sun, C. J. Takacs, S. R. Cowan, J. H. Seo, X. Gong, A. Roy and A. J. Heeger, *Adv. Mater.*, **2011**, 23, 2226-2230.

154 S. H. Park, A. Roy, S. Beaupré, S. Cho, N. Coates, J. S. Moon, D. Moses, M. Leclerc, K. Lee and A. J. Heeger, *Nat. Photonics*, **2009**, 3, 297-303.

155 Y.-J. Cheng, S.-H. Yang and C.-S. Hsu, *Chem. Rev.*, **2009**, 109, 5868-5923.

156 J. C. Hummelen, B. W. Knight, F. LePeq and F. Wudl, *J. Org. Chem.*, **1995**, 60, 532-538.

157 T. D. Anthopoulos, C. Tanase, S. Setayesh, E. J. Meijer, J. C. Hummelen, P. W. M. Blom and D. M. d. Leeuw, *Adv. Mater.*, **2004**, 16, 2174-2179.

158 M. M. Wienk, J. M. Kroon, W. J. Verhees, J. Knol, J. C. Hummelen, P. A. van Hal and R. A. Janssen, *Angew. Chem. Int. Ed.*, **2003**, 42, 3371-3375.

159 C. J. Lawrence, *Phys. Fluids*, **1988**, 31, 2786-2795.

160 K. Norrman, A. Ghanbari-Siahkali and N. B. Larsen, *Annu. Rep. Prog. Chem., Sect. C: Phys. Chem.*, **2005**, 101, 174-201.

161 W. W. Flack, D. S. Soong, A. T. Bell and D. W. Hess, *J. Appl. Phys.*, **1984**, 56, 1199-1206.

162 A. Budkowski, A. Bernasik, P. Cyganik, J. Rysz and R. Brenn, *e-Polymers*, **2002**, 006, 1-21.

163 G. Binnig, C. F. Quate and C. Gerber, *Phys. Rev. Lett.*, **1986**, 56, 930-933.

164 G. Binnig, H. Rohrer, C. Gerber and E. Weibel, *Phys. Rev. Lett.*, **1982**, 49, 57-61.

165 F. J. Giessibl, *Appl. Phys. Lett.*, **2000**, 76, 1470-1472.

166 O. Marti, B. Drake and P. K. Hansma, *Appl. Phys. Lett.*, **1987**, 51, 484-486.

167 S. A. C. Gould, K. Burke and P. K. Hansma, *Phys. Rev. B*, **1989**, 40, 5363-5366.

168 W. R. Bowen and N. Hilal, *Atomic Force Microscopy in Process Engineering*, Butterworth-Heinemann, Oxford, **2009**.

169 S. N. Magonov, V. Elings and M.-H. Whangbo, *Surf. Sci.*, **1997**, 375, L385-L391.

170 P. C. Zalm, *Vacuum*, **1994**, 45, 753-772.

171 W. C. Röntgen, *Sitzungsberichte der Physikalisch-Medicinisch Gesellschaft zu Würzburg*, **1895**, 132-141.

172 J. Drenth, *Principles of Protein X-ray Crystallography*, Springer-Verlag, New York, **2007**.

173 D. M. Mills, J. R. Helliwell, Å. Kvick, T. Ohta, I. A. Robinson and A. Authier, *J. Synchrotron Rad.*, **2005**, 12, 385.

174 P. Willmott, *An Introduction to Synchrotron Radiation*, John Wiley & Sons, Chichester, **2011**.

175 D. J. Griffiths, *Introduction to Electrodynamics, 4th edition*, Pearson Education Ltd, Harlow, **2013**.

176 A. Thompson, D. Attwood, E. Gullikson, M. Howells, K.-J. Kim, J. Kirz, J. Kortright, I. Lindau, Y. Liu, P. Pianetta, A. Robinson, J. Scofield, J. Underwood, G. Williams and H. Winick, *X-ray Data Booklet*, Lawrence Berkeley National Laboratory, University of California, Berkeley, **2009**.

177 D. Attwood, *Soft X-rays and Extreme Ultraviolet Radiation*, Cambridge University Press, Cambridge, **1999**.

178 O. Dhez, H. Ade and S. G. Urquhart, *J. Electr. Spectr. Rel. Phen.*, **2003**, 128, 85-96.

179 J. Stöhr, *NEXAFS Spectroscopy*, Springer-Verlag, Berlin, **1996**.

180 D. M. DeLongchamp, E. K. Lin and D. A. Fischer, *Proc. SPIE*, **2005**, 5940, 59400X.

181 G. Hähner, *Chem. Soc. Rev.*, **2006**, 35, 1244-1255.

182 H. Winick, *Synchrotron Radiation Research*, Plenum Press, New York, **1980**.

183 D. S. Germack, C. K. Chan, B. H. Hamadani, L. J. Richter, D. A. Fischer, D. J. Gundlach and D. M. DeLongchamp, *Appl. Phys. Lett.*, **2009**, 94, 233303.

184 A. L. D. Kilcoyne, T. Tyliszczak, W. F. Steele, S. Fakra, P. Hitchcock, K. Franck, E. Anderson, B. Harteneck, E. G. Rightor, G. E. Mitchell, A. P. Hitchcock, L. Yang, T. Warwick and H. Ade, *J. Synchrotron Rad.*, **2003**, 10, 125-136.

185 B. Watts and C. R. McNeill, *Macromol. Rapid Commun.*, **2010**, 31, 1706-1712.

186 A. Einstein, *Annalen der Physik*, **1905**, 322, 132-148.

187 C. S. Fadley, *J. Electron Spectrosc. Relat. Phenom.*, **2010**, 178-179, 2-32.

188 C. D. Wanger, W. M. Riggs, L. E. Davis and J. F. Moulder, *Handbook of X-ray Photoelectron Spectroscopy*, Perkin-Elmer Corporation, Eden Prairie, **1979**.

189 Lord Kelvin, *Philos. Mag.*, **1898**, 46, 82-120.

190 N. A. Surplice and R. J. D'Arcy, *J. Phys. E: Sci. Instrum.*, **1970**, 3, 477-482.

191 S. Sadewasser and T. Glatzel, *Kelvin Probe Force Microscopy*, Springer Verlag, Berlin, Heidelberg, **2012**.

192 I. D. Baikie, S. Mackenzie, P. J. Z. Estrup and J. A. Meyer, *Rev. Sci. Instrum.*, **1991**, 62, 1326-1332.

193 E. Abbe, *Archiv für Mikroskopische Anatomie*, **1873**, 9, 413-418.

194 L. de Broglie, PhD thesis, University of Paris, **1924**.

195 C. J. Davisson and L. H. Germer, *Phys. Rev.*, **1927**, 30, 705-741.

196 G. P. Thomson and A. Reid, *Nature*, **1927**, 119, 890.

197 H. Busch, *Annalen der Physik*, **1926**, 81, 974.

198 E. Ruska, *Rev. Mod. Phys.*, **1987**, 59, 627-638.

199 H. Lüth, *Solid Surfaces, Interfaces and Thin Films*, Springer Verlag, Berlin, Heidelberg, **2001**.

200 B. Fultz and J. Howe, *Transmission Electron Microscopy and Diffractometry of Materials*, Springer Verlag, Berlin, Heidelberg, **2007**.

201 L. Reimer, *Scanning Electron Microscopy: Physics of Image Formation and Microanalysis*, Springer Verlag, Berlin, Heidelberg, **1998**.

202 M. Dapor, *Transport of Energetic Electrons in Solids*, Springer, Cham, **2014**.

203 R. Erni, M. Rossell, C. Kisielowski and U. Dahmen, *Phys. Rev. Lett.*, **2009**, 102, 096101.

204 F. Liu, Y. Gu, X. Shen, S. Ferdous, H.-W. Wang and T. P. Russell, *Prog. Polym. Sci.*, **2013**, 38, 1990-2052.

205 L. Reimer, *Transmission Electron Microscopy: Physics of Image Formation and Microanalysis*, Springer Verlag, Berlin, Heidelberg, **1997**.

206 A. Braun, F. E. Huggins, N. Shah, Y. Chen, S. Wirick, S. B. Mun, C. Jacobsen and G. P. Huffman, *Carbon*, **2005**, 43, 117-124.

207 E. G. Rightor, A. P. Hitchcock, H. Ade, R. D. Leapman, S. G. Urquhart, A. P. Smith, G. Mitchell, D. Fischer, H. J. Shin and T. Warwick, *J. Phys. Chem. B*, **1997**, 101, 1950-1960.

208 A. P. Hitchcock, J. J. Dynes, G. Johansson, J. Wang and G. Botton, *Micron*, **2008**, 39, 311-319.

# Materials and Device Engineering for Efficient and Stable Polymer Solar Cells

With the increasing global demand for energy, solar cells provide a clean method for converting the abundant sunlight to electricity. Polymer solar cells can be made from a large variety of light-harvesting and electrically conducting molecules and are inexpensive to produce. They have additional advantages, like their mechanical flexibility and low weight, which opens opportunities for novel applications. In order for polymer solar cells to be more competitive, however, both the power conversion efficiencies and lifetimes need to further improve. One way to achieve this is to optimize the morphology of the active layer. The active layer of a polymer solar cell consists of electron donating and electron accepting molecules whose distribution in the bulk of the film is a major factor that determines the solar cell performance.

This thesis presents the use of complementary spectroscopy and microscopy methods to probe the local composition in the active layer of polymer solar cells. The stability of the active layer is studied and the interplay between the photo-degradation of the donor and acceptor molecules is investigated. Additionally, this thesis addresses how the interfacial layers between the active layer and the electrodes can influence device performance and stability.

ISBN 978-91-7063-736-0 (print)

ISBN 978-91-7063-739-1 (pdf)

ISSN 1403-8099

DOCTORAL THESIS | Karlstad University Studies | 2017:2